



Provided by the author(s) and University of Galway in accordance with publisher policies. Please cite the published version when available.

Title	An experimental and modeling study of propene oxidation. Part 1: Speciation measurements in jet-stirred and flow reactors
Author(s)	Burke, Sinéad M.; Metcalfe, Wayne; Herbinet, Olivier; Battin-Leclerc, Frédérique; Haas, Francis M.; Santner, Jeffrey; Dryer, Frederick L.; Curran, Henry J.
Publication Date	2014-06-20
Publication Information	Burke, SM, Metcalfe, W, Herbinet, O, Battin-Leclerc, F, Haas, FM, Santner, J, Dryer, FL, Curran, HJ (2014) 'An experimental and modeling study of propene oxidation. Part 1: Speciation measurements in jet-stirred and flow reactors'. Combustion And Flame, 161 :2765-2784.
Publisher	Elsevier ScienceDirect
Link to publisher's version	http://dx.doi.org/10.1016/j.combustflame.2014.05.010
Item record	http://hdl.handle.net/10379/6124
DOI	http://dx.doi.org/10.1016/j.combustflame.2014.05.010

Downloaded 2024-04-27T03:04:44Z

Some rights reserved. For more information, please see the item record link above.



1 An Experimental and Modeling Study of Propene
2 Oxidation. Part 1: Speciation Measurements in Jet-Stirred
3 and Flow Reactors.

4 Sinéad M. Burke^a, Wayne Metcalfe^a, Olivier Herbinet^b, Frédérique Battin-Leclerc^b,
5 Francis M. Haas^c, Jeffrey Santner^c, Frederick L. Dryer^c, Henry J. Curran^a

6 ^aCombustion Chemistry Centre, National University of Ireland, Galway, Ireland. ^bLaboratoire Réactions et Génie
7 des Procédés, CNRS, Nancy Université de Lorraine, CNRS UPR 3349, BP 20451, ^cDepartment of Mechanical and
8 Aerospace Engineering, Princeton University, Princeton, NJ, United States

9
10 **Abstract**

11 Propene is significant component of Liquefied Petroleum Gas (LPG) and an intermediate in
12 the combustion of higher order hydrocarbons. To better understand the combustion
13 characteristics of propene, this study and its companion paper present new experimental data
14 from jet-stirred (JSR) and flow reactors (Part I) and ignition delay time and flame speed
15 experiments (Part II).

16 Species profiles from JSR experiments are presented and were obtained at near-atmospheric
17 pressure over a temperature range of 800–1100 K and for equivalence ratios from $\phi = 0.64$ to
18 2.19. The new JSR data were obtained at lower dilution levels and temperatures than previously
19 published. Also reported are species profiles from two high-pressure flow reactor facilities: the
20 Princeton Variable Pressure Flow Reactor (VPFR) and the High Pressure Laminar Flow Reactor
21 (HPLFR). The VPFR experiments were conducted at pressures of 6–12.5 atm, in the temperature
22 range 843–1020 K and at equivalence ratios of 0.7–1.3. The HPLFR experiments were conducted
23 at 15 atm, at a temperature of 800 K and at equivalence ratios of 0.35–1.25. The flow reactor data
24 is at higher pressures and lower temperatures than existing data in the literature.

25 A detailed chemical kinetic mechanism has been simultaneously developed to describe the
26 combustion of propene under the experimental conditions described above. Important reactions
27 highlighted via flux and sensitivity analyses include: hydrogen atom abstraction from propene by
28 molecular oxygen, hydroxyl, and hydroperoxyl radicals; allyl-allyl radical recombination; the
29 reaction between allyl and hydroperoxyl radicals; and the reactions of 1- and 2-propenyl radicals
30 with molecular oxygen. The current mechanism accurately predicts the combustion
31 characteristics of propene across the range of experimental conditions presented in this study,
32 from jet-stirred and flow reactors and for ignition delay times and flame speed measurements
33 presented in Part II. In comparison to a previous mechanism, AramcoMech 1.3, the current
34 mechanism results in much improved performance, which highlights the importance of the new
35 experimental data in constraining the important reactions.

36 **Keywords:** Propene, jet-stirred reactor, flow reactor, chemical kinetics, mechanism
37 development

42

43 1. Introduction

44 Propene is a key intermediate in the combustion of higher alkanes, such as propane, *n*-butane,
45 *n*-heptane, and *iso*-octane, as it is a product of alkyl radical decomposition. It is a significant
46 component of Liquefied Petroleum Gas (LPG) and due to the shale gas “revolution” there may be
47 a surplus of LPG [1] available as an alternative energy source. Therefore, it is important to
48 understand the combustion characteristics of propene. It may also serve as an archetypal alkene
49 fuel. Following H-atom abstraction from propene, a resonantly stabilized allyl radical is formed.
50 Allylic species are implicated in the formation of aromatic and subsequent poly-aromatic
51 hydrocarbon species [2], which are the major precursors for soot emissions. Strategies for
52 mitigating pollutant formation in advanced combustion systems depend, in part, on
53 understanding the oxidation chemistry of alkenes such as propene.

54 Despite its importance, there is a lack of experimental data available in the literature for
55 propene at low temperatures (600–1000 K) and high pressures (≥ 10 atm). There are two studies
56 in a jet-stirred reactor (JSR) from Dagaut and co-workers [3, 4] for propene oxidation. The
57 earlier study [3] investigated propene oxidation as a function of residence time over the
58 temperature range 900–1200 K in the pressure range 1–8 atm. The later atmospheric pressure
59 study by Le Cong et al. [4] investigated the oxidation of pure propene and its oxidation in the
60 presence of CO₂ and H₂O over the temperature range 950–1450 K. Previous flow reactor studies
61 include the investigation by Davis et al. [5], who studied atmospheric pressure propene pyrolysis
62 and oxidation ($\phi = 0.7$ –1.4) as a function of residence time over the temperature range 1181–
63 1210 K.

64 There are several mechanisms in the literature that can be used to simulate propene
65 combustion [3, 5, 6–12,15]. Westbrook and Pitz [6] developed a detailed chemical kinetic
66 mechanism to describe the oxidation and pyrolysis of propane and propene. Dagaut et al. [3]
67 presented a chemical kinetic reaction mechanism capable of reproducing their speciation results,
68 with an updated version published four years later [15]. Their mechanism built on previous
69 studies by Warnatz [13] and Westbrook [6] and included additional rate constants for the
70 reactions of propene with hydroxyl and hydroperoxyl radicals from Baldwin and Walker [14].

71 Wilk et al. [7] developed a mechanism capable of simulating low temperature (530–740 K)
72 static reactor data. It is one of the few mechanisms in the literature developed to simulate the
73 low-temperature oxidation of propene. Rate constants were adopted from the literature where
74 available. Otherwise, estimates were made by analogy to similar reactions. A region of negative
75 temperature coefficient behavior was predicted by the model and agreed with observed
76 experimental behavior; however, the authors stated that they “*did not know if the slight*
77 *deviations in the experimental data are actual indications of NTC behavior or if they are data*
78 *scatter.*” The study by Simonyan and Mantashya [8] also reports conflicting evidence of propene
79 NTC behavior. The presence of NTC for propene is inconclusive and it is addressed in Part II
80 [10] of the current work.

81 Tsang [9] published a review of evaluated and estimated rate constants for propene
82 unimolecular decomposition reactions, H-atom abstraction reactions, and reactions of the allyl
83 radicals formed therein. Rate constant recommendations originated from experimental
84 measurements where available or were otherwise estimated.

85 More recently, Davis et al. [5] presented a chemical kinetic mechanism to describe the high-
86 temperature kinetics of propane, propene, allene, and propyne. The mechanism included rate
87 constants adopted from the literature and calculated via ab initio quantum mechanical and Rice-
88 Ramsperger-Kassel-Marcus (RRKM) analyses. It was validated against the flow reactor and

89 flame speed data presented in their study, in addition to flame speed targets from the literature.

90 The propene oxidation mechanism presented by Heyberger et al. [11] was generated using the
91 EXGAS code. The mechanism was validated against speciation data from a JSR and low-
92 temperature static reactor data. Braun-Unkhoff et al. [12] presented a propene sub-mechanism
93 validated against laminar flame speed and ignition delay time data. Rate constants for both
94 propene pyrolysis and oxidation sub-mechanisms were adopted from the literature [5, 9, 16–18].

95 Table 1: Jet-stirred reactor and flow reactor data for propene oxidation.

Reactor	T (K)	p (atm)	ϕ	Dilution	Ref.
Data for propene oxidation available in the literature					
Static	580–715	0.79	0.8–2.0	“in air”	[7]
JSR	900–1200	1–8	0.15–4.0	> 95% N ₂	[3]
JSR	950–1200	1.0	0.5–2.0	> 95% N ₂	[4]
FR	950–1200	1.0	pyrolysis	> 95% N ₂	[5]
FR	1180–1210	1.0	0.5–2.0	> 95% N ₂	[5]
Data for propene oxidation obtained in this study					
JSR	800–1100	1.05	0.64–2.19	> 87–95% He	
FR	800	15.0	0.35–1.25	> 90% N ₂	
FR	840–1020	6.0–12.5	0.7–1.31	> 97% N ₂	

96 2. Experimental Methods

97 Table 1 compares the experimental conditions investigated during this study to those of
98 previous studies. The present JSR data were obtained under similar conditions to previous studies
99 from Dagaut and co-workers [3, 4]. However, the mixtures investigated in this study used a
100 higher concentration of reactants than the previous studies (for example, we used $\approx 1.62\%$ C₃H₆
101 while Dagaut and co-workers [3, 4] used 0.15% C₃H₆ for the same equivalence ratio). The more
102 concentrated mixtures facilitated measurement of reactivity in the lower temperature range
103 compared to the previous studies. Profiles for additional species such as allene, propyne, butene,
104 acrolein, and 1,5-hexadiene were also reported. These species proved useful for mechanism
105 development; for example, the detection of butene and 1,5-hexadiene indicated the importance of
106 certain radical-radical recombination reactions. New data from the flow reactors were obtained at
107 lower temperatures and higher pressures than the previous studies. The experimental data are
108 compared with predictions of a chemical kinetic mechanism and all simulations presented in this
109 study were performed using the CHEMKIN-PRO [19] suite of programs.

110 2.1. Jet-stirred reactor

111 Experiments were performed in a spherical fused silica jet-stirred reactor operated at constant
112 temperature and pressure located at the Laboratoire Réactions et Génie des Procédés (LRGP) at
113 the University of Lorraine in Nancy, France. The experimental apparatus has been described
114 previously [20, 21] and only the main features are discussed here. Stirring is achieved by
115 turbulent jets flowing through an injection cross located at the center of the sphere. The rapid
116 mixing achieves spatial temperature and concentration homogeneity within the reactor when it is
117 operated at a steady state. The internal volume of the reactor is 92 cm³ and it has been designed
118 to operate with residence times of 0.5–5.0 s [22]. In order to avoid temperature gradients within
119 the reactor it is preceded by an annular pre-heater, where the temperature of the vapor mixture is
120 increased to the temperature of the reactor before entering it. The residence time in the preheater
121 is long enough to heat the gas to the reaction temperature due to the annular geometry. The
122 residence time of the gas inside the pre-heater is 1% of the total residence time in the reactor.
123 Heating is achieved with independent ‘Thermocoax’ resistance heaters coiled around the

124 different zones of the experimental set up. The reaction temperature is measured using a type K
125 thermocouple. The thermocouple is located inside the intra-annular space of the pre-heating
126 zone, the extremity of which is on the level of the injection cross. The uncertainty in the
127 temperature measurement is ± 5 K.

128 Reaction products were analyzed using online gas chromatography. In total, three gas
129 chromatographs were used to quantify a wide range of products. Light species such as oxygen,
130 carbon monoxide, carbon dioxide, and C_1 – C_2 hydrocarbons were analyzed using a gas
131 chromatograph fitted with a sampling valve, a carbosphere packed column, and two detectors: a
132 thermal conductivity detector (TCD) for oxygen atom containing species and a flame ionization
133 detector (FID) for hydrocarbons. Helium was used as a carrier gas in the GC as it was also used
134 as a diluent gas in the experiments. A second gas chromatograph was used for the quantification
135 of C_1 – C_6 hydrocarbons and was fitted with a sampling valve, a capillary Plot Q column, and an
136 FID, with the same carrier gas. Despite the use of these two gas chromatographs, important
137 species such as formaldehyde and water could not be quantified. The calibration of the facilities
138 was performed using gaseous standards provided by Messer and Air Liquide. For species not
139 directly calibrated from standards, the effective carbon number method was used to calculate the
140 calibration coefficient [23]. The uncertainty in the mole fraction was estimated at $\pm 5\%$ (less for
141 species directly calibrated). The detection limit was about 1 ppm for hydrocarbons detected with
142 the FID. The detection limit in the measurements was 10 and 100 ppm for CO and CO_2 ,
143 respectively (with the TCD). Species identification was performed with a third gas
144 chromatograph coupled to a mass spectrometer. The mass spectra of most species were included
145 in the NIST08 spectra database [24]. The residence time for each mixture was 2.0 s and the
146 pressure was fixed to 106.7 kPa (800 Torr). The exact compositions of the mixtures studied are
147 included in Table 2.

148 Concentration profiles of stable species such as oxygen, carbon monoxide, carbon dioxide,
149 methane, ethylene, acetylene, ethane, propene, allene, propyne, acetaldehyde, butene isomers,
150 1,3-butadiene, methyl oxirane, acrolein, propanal, acetone, benzene, 1,5-hexadiene were
151 measured during the experiments.

152 Table 2: Experimental conditions for the JSR. $\tau = 2.0$ s and $p = 1.05$ atm.

ϕ	C_3H_6 (%)	O_2 (%)	He (%)
0.64	1.65	11.60	86.75
1.10	1.62	6.81	91.57
1.68	1.68	4.50	93.82
2.19	1.64	3.38	95.28

153 2.1.1. *Jet-stirred reactor simulation*

154 The CHEMKIN-PRO steady state solver was used for simulations and included isothermal,
155 isobaric assumptions.

156 2.2. *Flow reactor*

157 Experiments were conducted in two flow reactors at Princeton University, the Variable
158 Pressure Flow Reactor (VPFR) and the High Pressure Laminar Flow Reactor (HPLFR).

159 2.2.1. *Flow reactor simulation*

160 Simulations of VPFR experiments were performed assuming a 0-D system with isobaric and
161 adiabatic approximations. In order to compare model predictions to time history measurements
162 performed in the Princeton VPFR, the simulations are subject to a time-shifting procedure [26].

163 The time-shifting technique has been thoroughly discussed by Zhao et al. [27]. The HPLFR is
164 simulated using an isothermal assumption and is also subject to a time-shifting procedure, which
165 is further discussed below.

166 2.2.2. Princeton Variable Pressure Flow Reactor (VPFR)

167 The design, instrumentation and experimental methodology of this apparatus have been
168 discussed in detail previously [27–29] and are therefore only briefly reviewed here. The carrier
169 gas (N₂) is heated and mixed with oxygen as it enters the reactor tube. The carrier gas/oxygen
170 mixture flows around a baffle plate into a gap serving as the entrance to a diffuser. The
171 remaining reactant (fuel) is diluted with N₂ and injected radially outward into this gap where it
172 rapidly mixes with the carrier gas and oxygen, establishing the initial reaction temperature for the
173 experiment. The reacting mixture exits the diffuser into the test section. Near the exit of the test
174 section, a sampling probe is positioned on the reactor centerline to continuously extract and
175 convectively quench a small percentage of the flow. At the same axial location, the local reaction
176 gas temperature is measured with a silica-coated R-type thermocouple. The sample gas flows via
177 heated Teflon lines to analytical equipment that includes a Fourier transform infrared
178 spectrometer (FTIR), an electrochemical O₂ analyzer, and a pair of non-dispersive infrared
179 analyzers for CO and CO₂. Small volumes of the sample flow can also be stored in heated multi-
180 port sample storage valve systems that can be transferred to a GC for off-line analysis. C₃H₆,
181 H₂O, CH₂O and C₂H₂ were measured on-line using FTIR spectrometry. C₂H₄, CH₄, C₂H₆,
182 isobutene and 1,3-butadiene were measured using sample storage and subsequent off-line GC
183 analysis. Species profiles for O₂, CO, CO₂, H₂, CH₂O, CH₄, C₂H₄ and C₃H₆ are reported in
184 Section 4.2.1.

185 Table 3 contains selected mixtures studied; further experiments are included in the
186 Supplementary Material.

187 Table 3: Experimental conditions studied in the VPFR^a.

p (atm)	T (K)	ϕ	C ₃ H ₆ (%)	O ₂ (%)	N ₂ (%)
8.0	955	0.94	0.31	1.49	98.20
10.0	942	1.37	0.34	1.10	98.56
12.5	843	0.71	0.33	2.10	97.57

^aadditional conditions considered in Supplementary Material

188 2.2.3. High Pressure Laminar Flow Reactor (HPLFR)

189 The HPLFR is a new reactor facility developed to measure both fundamental chemical
190 kinetic rate coefficients as well as systems-type reaction features for species of interest to
191 combustion and gas phase reaction kinetics. This facility is described in detail in the thesis of
192 Haas [30], which also describes its favorable validation performance in measuring relatively well
193 established rate coefficients for the reactions $\dot{H} + O_2(+M) \rightarrow \dot{H}O_2(+M)$ (where M = N₂ and Ar) and
194 $\dot{H} + NO_2 \rightarrow NO + \dot{O}H$. Accordingly, only a brief description of the system is presented below.

195 The HPLFR essentially consists of a 38 mm O–D stainless steel pressure shell enclosed by a
196 PID-thermostatted three-zone tube furnace. This pressure shell itself encloses one of several
197 coaxial reactor duct designs. In the present experiments, the quartz test section of the duct is of
198 cylindrical geometry and has an internal diameter of 10 mm. The duct is fed by a steady flow of
199 premixed, preheated gaseous reactants supplied from calibrated mass flow controllers. Under
200 conditions favoring reaction, premixed gas feed converts into products as it travels along the duct
201 and subsequently exhausts from the reactor. A back pressure regulator on the exhaust line

202 controls the pressure both inside the duct and in the annular space between the duct and the
203 pressure shell. This feature automatically maintains pressure equilibrium across the fragile quartz
204 duct wall. The reactor facility accommodates relatively high pressures (30 atm) and temperatures
205 ranging from approximately 500–1000 K.

206 A small fraction of the reacting flow in the duct is extracted from the test section using a hot
207 water-cooled, convection quench probe with integrated thermocouple. This continuous, quenched
208 sample flow passes through heated Teflon transfer lines (100°C) to a pressure-regulated online
209 Inficon 3000 micro gas chromatograph, which permits identification and quantification of stable
210 species of interest. Stable species mole fractions are determined from chromatogram area
211 responses and retention times measured from dilutions of calibration standards. A screw drive
212 translates the probe axially through the duct, enabling sample collection at different axial
213 locations along the length of the test section.

214 The steady laminar reacting flow field in the HPLFR (or any hydrodynamically similar
215 facility) may support both axial and radial gradients in velocity, species mole fraction, and
216 temperature. However, modelling [30] of the specific axisymmetric reacting flow conditions
217 describing the present experiments shows that the experiments are reasonably well characterized
218 by simple steady 1-D axial plug flow, particularly for low fuel conversion where transport
219 gradients are small. Diagnostic experiments described in [30], as well as demonstrated HPLFR
220 validation against literature rate coefficients for $\dot{\text{H}}+\text{O}_2(+\text{M})\rightarrow\dot{\text{H}}\text{O}_2(+\text{M})$ and $\dot{\text{H}}+\text{NO}_2\rightarrow\text{NO}+\dot{\text{O}}\text{H}$
221 suggest negligible influence of wall reactions on the quartz duct for species spanning a broad
222 spectrum of reactivities (i.e., $\dot{\text{H}}$ and $\dot{\text{O}}\text{H}$, $\dot{\text{H}}\text{O}_2$, NO_x , and stable reactants/products).
223 Consequently, a mean velocity-axial displacement relationship gives the effective 0-D
224 homogeneous chemistry residence time in the test section, subject to additional treatment
225 discussed in Section 4.2. It is important to note that this simplification of the complex interaction
226 of the chemical source term with thermal and species diffusion and the laminar flow-field applies
227 only for specific experimental conditions, and does not generalize to any conditions beyond those
228 reported here.

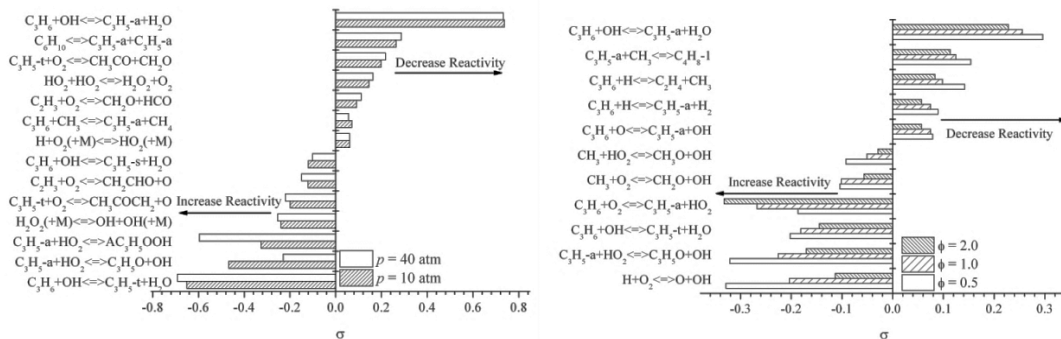
229 Experimental composition measurements of the reacting flow were obtained by convection
230 quenched sampling at discrete axial locations, followed by micro GC analysis of the flowing
231 sample gases. Species profiles were reported for stable species including C_3H_6 , O_2 , CO , CO_2 , and
232 H_2O . The micro GC was calibrated to measure H_2 , CH_4 , C_2H_6 , $\text{C}_3\text{H}_4\text{-a}$ (allene), and $\text{C}_3\text{H}_4\text{-p}$
233 (propyne) in addition to the species reported below. Mole fractions of these additional species
234 were below detection/quantification limits of tens of ppm for all experiments; an observation
235 which is itself mechanistically constraining. The retention time for CH_2O was identified using
236 formalin solution, but the mole fraction could not be accurately, independently quantified. For
237 the $\phi = 0.35$ and 0.5 experiments, H_2O and CH_2O measurements have been excluded as a result
238 of sample condensation observed during the experiments. Effects of this condensation on the
239 mole fractions of other reported species was shown to be negligible.

240 Table 4: Experimental conditions studied in the HPLFR, $T = 800$ K and $p = 15.0$ atm.

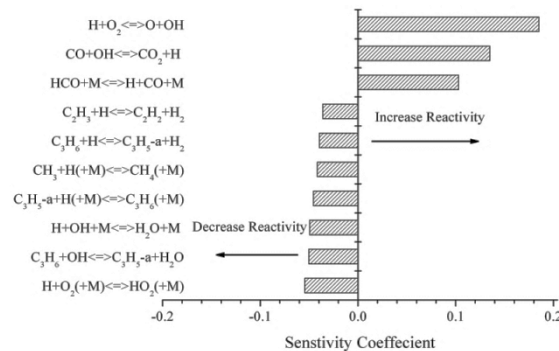
ϕ	C_3H_6	O_2	N_2
0.35	0.40	5.14	94.45
0.50	0.45	4.05	95.50
1.00	0.50	2.50	97.25
1.25	0.62	2.25	97.13

242 3. Chemical kinetic mechanism development

243 The foundation of the detailed kinetic mechanism presented in this study is based on recent
 244 publications. The H_2/O_2 sub-mechanism is adopted from the study of K eromn es et al. [31] and
 245 the C_1/C_2 sub-mechanism (AramcoMech 1.3) adopted from the recent publications of Metcalfe
 246 and co-workers [32–36]. AramcoMech 1.3 included rate constants for C_3 and C_4 species such as
 247 propene, allene, propyne, and 1,3-butadiene, adopted from the study by Laskin et al. [41], as well
 248 as rate constants for the butane isomers from the studies of Healy and co-workers [37–40]. Rate
 249 constants for the aromatic sub-mechanism were included from the toluene study by Metcalfe et
 250 al. [42]. However, despite AramcoMech 1.3 [32] containing mechanistic structure,
 251 thermochemistry, and rate parameters for reactions of larger hydrocarbon species and radicals,
 252 the model was not extensively validated for species larger than C_2 . We aim to improve the
 253 predictive power of the mechanism for the range of experiments presented herein. Changes to
 254 both kinetic and thermochemical data have taken place and these changes are discussed in detail
 255 below.



256 (a) Brute force sensitivity analysis of C_3H_6 /air IDTs.
 257 $\phi = 1.0$, $T = 950$ K.
 258 (b) Brute force sensitivity analysis of C_3H_6 /air
 IDTs. $p = 10$ atm, $T = 1250$ K.



259 (c) Flame speed sensitivity analysis of C_3H_6 /air laminar flame at 1 atm.
 260

261 Figure 1 : Important reactions for propene oxidation highlighted by brute force, and flame speed
 262 sensitivity analyses carried out during the course of this study.

263 During its development, the mechanism was validated against experimental targets at a variety
 264 of experimental conditions. The speciation measurements presented in this study and ignition and
 265 flame speed data presented in Part II [10] were all tested concurrently. Important reactions for
 266 propene oxidation in the JSR and flow reactor were highlighted by flux analyses as shown in
 267 Figs. 18 and 26. In order to highlight the important reactions for propene oxidation over the

268 entire range of conditions studied, sensitivity analyses for reflected shock ignition delay times
269 (IDTs) and laminar flame speed data [10] are included in Fig. 1.

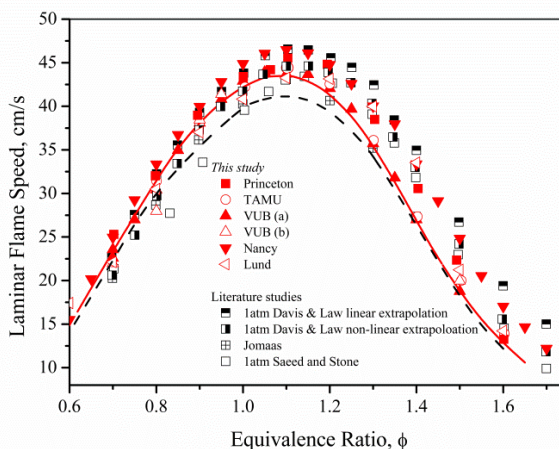
270 The choice of rate constants for many of the important reactions highlighted in Fig. 1 are
271 discussed and explained below. The Arrhenius coefficients for all of the important reactions are
272 provided in a table in the Supplementary Material. The complete kinetic mechanism,
273 thermochemistry and transport files are available to download at
274 <http://c3.nuigalway.ie/mechanisms.html>.

275 The mechanism developed in this work results in improved performance against a variety of
276 experimental data. The most significant improvement can be seen when compared against data at
277 lower temperatures and at higher pressures, where the new experimental data presented in this
278 study from shock tubes, RCMs, JSRs, flow reactors and flame speeds have provided important
279 validation targets. The performance of the mechanism presented in this study is compared with
280 the performance of selected mechanisms available in the literature [5,12,32] in the
281 Supplementary Material.

282 3.1. $C_3H_6 (+M) \leftrightarrow Products$

- 283 • $\dot{C}_3H_5\text{-a} + \dot{H} (+M) \leftrightarrow C_3H_6 (+M)$
- 284 • $\dot{C}_2H_3 + \dot{C}H_3 (+M) \leftrightarrow C_3H_6 (+M)$

285 Propene/air laminar flame speeds are sensitive to propene decomposition to allyl radical and a
286 hydrogen atom, Fig. 1(c). This rate constant, which we describe in the recombination direction,
287 has been adopted from the study by Tsang [9]. However, in order to improve agreement with
288 flame speed measurements presented in Part II [10], the rate constant for the recombination of
289 allyl radical and atomic hydrogen was reduced by a factor of two, this is within the stated
290 uncertainty [9]. Figure 2 shows that reducing the rate of this reaction increased the flame speed
291 by approximately 2 cm s^{-1} . This reduction had little or no effect on mechanism performance
292 against other experimental targets. Flames are less sensitive to the channel producing vinyl and
293 methyl radicals, and this rate coefficient is adopted unchanged from the study by Tsang.



294 Figure 2 Effect of changing the $\dot{C}_3H_5\text{-a} + \dot{H} (+M) \leftrightarrow C_3H_6 (+M)$ rate constant on predictions of 1
295 atm flame speeds (red symbols new data [10]). - - - Tsang [9], — [9] reduced by a factor of two.
296

297 3.2. $C_3H_6 + \dot{R} \leftrightarrow Products$

298 Propene can undergo hydrogen atom abstraction from three sites: the methyl site forming the
299 resonantly stabilized allyl radical ($\dot{C}_3H_5\text{-a}$), the other terminal carbon resulting in the formation
300 of a vinylic radical propen1-yl ($\dot{C}_3H_5\text{-s}$); and the central carbon to give propen-2-yl ($\dot{C}_3H_5\text{-t}$).

301 Hydrogen atom abstraction resulting in the formation of the allyl radical is generally dominant as
302 it is the weakest C–H bond in propene. Abstraction reactions by various radicals are discussed in
303 the following subsections.

304 3.2.1. $C_3H_6 + \dot{H} \leftrightarrow Products$

305 Sensitivity analyses, Fig. 1(b), and flux analyses, Figs. 18 and 26, have identified the
306 importance of reactions between propene and atomic hydrogen. At high and intermediate
307 temperatures (>1200K) hydrogen atom addition to propene acts to inhibit reactivity, as it
308 competes with the main chain branching and reactivity promoting reaction, $\dot{H} + O_2 \leftrightarrow \dot{O} + \dot{O}H$.
309 As temperatures decrease (< 800K), $C_3H_6 + \dot{H}$ reactions promote reactivity. Both *n*- and *iso*-
310 propyl radicals undergo low-temperature chemistry reactions via reaction with molecular oxygen
311 to form RO_2 radicals, which after a series of isomerization reactions and further molecular
312 oxygen addition reactions, eventually lead to the formation of several radicals, thereby promoting
313 reactivity.

314 Previously [32], an estimated high-pressure limit rate constant for the alkyl radical
315 decomposition channels from Curran [44] and an estimated rate constant from the study of Tsang
316 [9] for the ethylene and methyl radical channel were included in the mechanism. In this study,
317 the rate constants for hydrogen atom addition to and abstraction from propene have been adopted
318 from the recent theoretical study of Miller and Klippenstein [45]; they used CCSD(T)/ccpVTZ
319 (for the non-abstraction reactions) and the MP2/6-311++G(d,p) methods (for the abstraction
320 reactions).

321 Miller and Klippenstein provided pressure dependent rate constants for the reactions that
322 occur on the \dot{C}_3H_7 potential energy surface. They stated that the dominant product sets for $C_3H_6 +$
323 \dot{H} are the formation of *iso*- \dot{C}_3H_7 and *n*- \dot{C}_3H_7 radicals, and $C_2H_4 + \dot{C}H_3$. In addition to the reaction
324 between methyl radical and ethylene that results in the formation of *n*- \dot{C}_3H_7 radicals, Miller and
325 Klippenstein provided rate constants for the abstraction channel that results in the formation of a
326 vinyl radical and methane. The total addition rate constant adopted in this study is larger than the
327 previous total rate constant, but its inclusion had only a small effect on the mechanism
328 performance for propene. Inclusion of these rate constants has a significant effect on the
329 performance of the mechanism against ethylene targets, as shown in the Supplementary Material.

330 3.2.2. $C_3H_6 + \dot{C}H_3 \leftrightarrow Products$

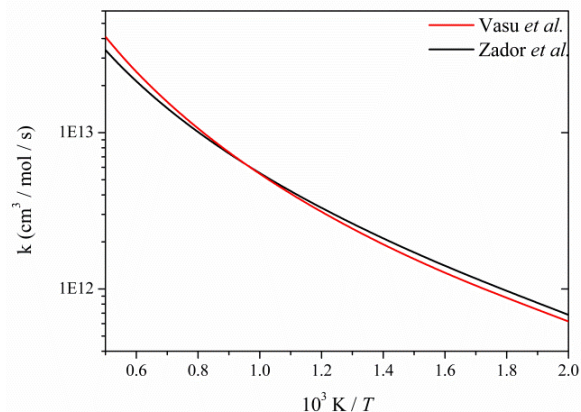
331 Methyl radical can abstract a hydrogen atom from propene from any of the three sites,
332 however, only the channel producing methane and an allyl radical was observed to be
333 competitive. This reaction is predicted to be a significant source of methane detected in the JSR.
334 The recommendation in this study is an estimated rate constant from Tsang [9].

335 We did not observe sensitivity to methyl radical addition to propene to form \dot{C}_4H_9 radicals
336 during this study. However, rate constants for methyl radical addition to propene resulting in the
337 formation of *iso*- and 2-butyl radicals are included from Curran [44].

338 3.2.3. $C_3H_6 + \dot{O}H \leftrightarrow Products$ 339 *Abstraction by $\dot{O}H$*

340 The hydroxyl radical is a dominant reactive radical in combustion processes. It is highly
341 reactive, which is due in part to the exothermicity of water formation which is relatively large at
342 $-57.80 \text{ kcal mol}^{-1}$. Ignition delay times are highly sensitive to the branching ratio between the
343 three abstraction channels, as seen in Fig. 1(a). The allyl radical producing channel is the most
344 inhibiting of the three, it results in the consumption a highly reactive hydroxyl radical and the
345 formation of a far less reactive resonantly stabilized allyl radical. The \dot{C}_3H_5 -a radical can readily
346 undergo radical-radical recombination with itself or with methyl radicals via chain terminating
347 reactions which inhibit reactivity. The channels forming \dot{C}_3H_5 -t and \dot{C}_3H_5 -s radicals promote

348 reactivity. These radicals react with molecular oxygen via chain branching pathways.



349 Figure 3: Total $C_3H_6 + \dot{O}H$ abstraction rate constant, Vasu et al. [46] and Zádor et al. [47].

350 Rate constants for the reactions of propene with hydroxyl radicals have been adopted from the
351 experimental study of Vasu et al. [46], who measured the rate constant in a shock tube using laser
352 absorption. Zádor et al. [47] investigated these reactions theoretically employing
353 RQCISD(T)/ccpV ∞ Z//B3LYP/6-311++G(d,p) quantum chemical calculations. The total rate
354 constants recommended in these two recent studies are in good agreement as shown in Fig. 3; up
355 to 1500 K they agree within 10% and are within 20% of each other between 1500 and up to 2000
356 K. Unlike the study of Vasu et al., the theoretical study of Zádor et al. provided a branching ratio
357 which we have adopted.

358 3.2.4. $\dot{O}H$ addition to C_3H_6

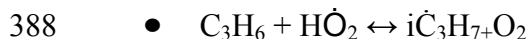
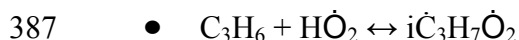
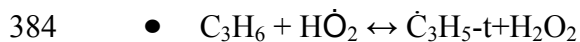
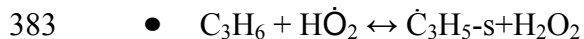
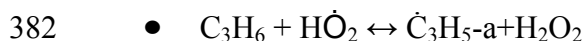
- 359 • $C_3H_6 + \dot{O}H \leftrightarrow \dot{C}_3H_6OH1-2$
- 360 • $C_3H_6 + \dot{O}H \leftrightarrow \dot{C}_3H_6OH2-1$
- 361 • $C_3H_6 + \dot{O}H \leftrightarrow C_3H_5OH + \dot{H}$
- 362 • $C_3H_6 + \dot{O}H \leftrightarrow C_2H_3OH + \dot{C}H_3$
- 363 • $C_3H_6 + \dot{O}H \leftrightarrow iC_3H_5OH + \dot{H}$
- 364 • $C_3H_6 + \dot{O}H \leftrightarrow sC_3H_5OH + \dot{H}$
- 365 • $C_3H_6 + \dot{O}H \leftrightarrow CH_3CHO + \dot{C}H_3$

366 In this study, rate constants for the above reactions have been adopted from the theoretical
367 study of Zádor et al. [47]. Zádor et al. stated a 50:50 branching ratio for hydroxyl radical
368 addition to propene to form the two \dot{C}_3H_7O radicals via addition to the terminal or central carbon
369 atom. Addition to the terminal carbon results in the formation of the C_3H_6OH1-2 radical
370 ($CH_3\dot{C}HCH_2OH$), which reacts with molecular oxygen to form propanal and a hydroperoxyl
371 radical. Addition to the central carbon results in the formation of the C_3H_6OH2-1 radical
372 ($CH_3CH(OH)\dot{C}H_2$) which also reacts with O_2 and results in the formation of acetone and a
373 hydroperoxyl radical. In this study we use a branching ratio of 75:25 in favor of addition to the
374 terminal carbon. This is consistent with the experimental study by Loison et al. [48], who stated
375 that $72 \pm 16\%$ of $\dot{O}H$ addition to propene proceeds via addition to the terminal C atom. The rate
376 constants for the consumption of these radicals with molecular oxygen have been adopted from
377 the study by Frassoldati et al. [49]. Above 1000 K, hydroxyl radical addition to propene is not a
378 major consumption pathway and only a small amount ($\approx 5\%$) of the $C_3H_6 + \dot{O}H$ flux proceeds via

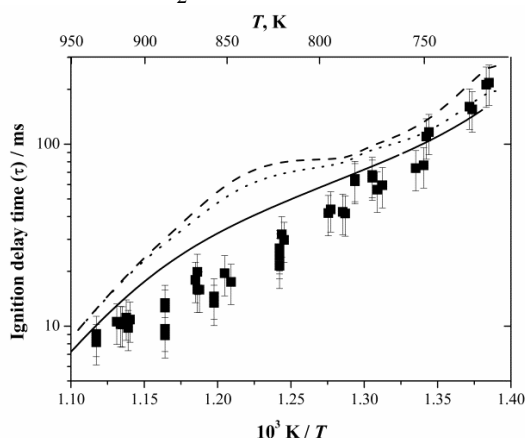
379 addition reactions, resulting in the formation of vinyl alcohol and a methyl radical.

380

381 3.2.5. $C_3H_6 + HO_2 \leftrightarrow Products$



390 Reactions that involve the hydroperoxyl radical are most influential at elevated pressures and
 391 lower temperatures. Under these conditions stabilization of $\dot{H} + O_2 (+M) \leftrightarrow HO_2 (+M)$ is favored
 392 over the chain branching reaction $\dot{H} + O_2 \leftrightarrow \dot{O} + \dot{OH}$.



393 Figure 4: Effect of changing the $C_3H_6 + HO_2$ rate constants on predicted RCM ignition delay
 394 times for fuel/air, $p = 40$ atm, $\phi = 1$ mixture (Mix 11 [10]). — *This study*, --- previous [32],
 395 Zádor et al. [51] abstraction rate constant.

396 The rate constants for the addition and abstraction reactions of propene and hydroperoxyl
 397 radicals are adopted from the theoretical study of Zádor et al. [51]. The addition rate constants
 398 are pressure dependent. The rate constant for the abstraction reaction forming allyl radical was
 399 decreased by a factor of 2.5. This was necessary in order to best match experimental data, Fig. 4.
 400 The rate constant for the abstraction reaction of propene and a hydroperoxyl radical was
 401 previously estimated based on analogy to the reaction of toluene with hydroperoxyl radical [50],
 402 while the previous addition reaction rate constant was adopted from Baldwin and et al. [52].

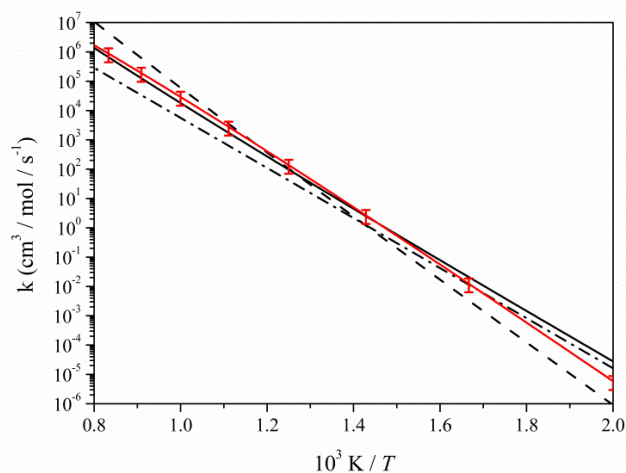
403 3.2.6. $C_3H_6 + O_2 \leftrightarrow Products$

404 For hydrogen atom abstraction by molecular oxygen, only the reaction resulting in the
 405 formation of allyl and hydroperoxyl radicals was found to be sensitive, the other pathways were

406 not competitive.

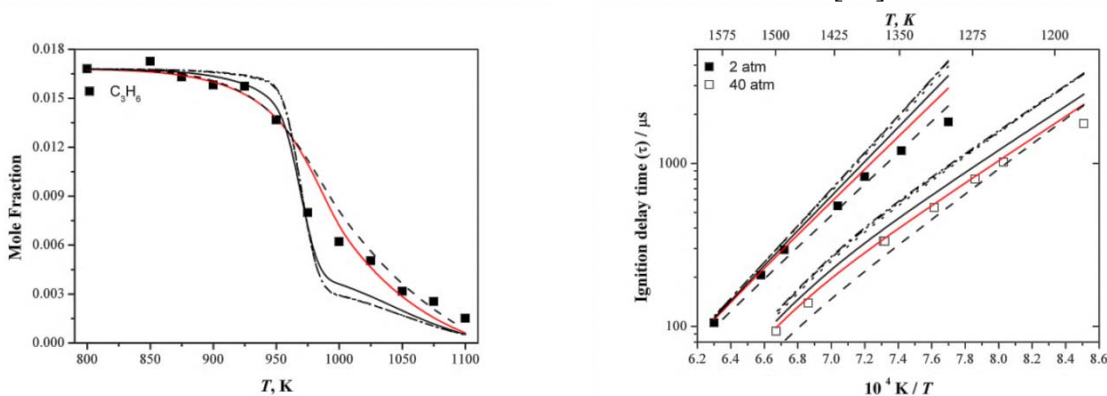
407 Baulch et al. [53] and Tsang [9] reported rate constants based on extensive literature reviews.
408 Barbé et al. [54] studied this reaction experimentally. They carried out a measurement at 800 K
409 using a conventional static system and their results showed good agreement with a previous
410 experimental measurement from Stothard and Walker [55], who measured rate constants in the
411 temperature range 673–793 K. Goldsmith et al. [56] investigated this reaction theoretically as
412 part of their study of the reactions between allyl and hydroperoxyl radicals. In order to directly
413 compare this rate constant, it was written in the opposite direction using the CHEMRev software
414 [57].

415 This reaction has a very similar $\Delta_r H^\circ$ to the reaction of toluene and molecular oxygen forming
416 benzyl and hydroperoxyl radicals. It also has the same number of hydrogen atoms available for
417 abstraction. As discussed by Carstensen and Dean [59], there is a linear relationship between
418 barrier height and heat of reaction for hydrogen atom abstraction from C–H bond types. It could
419 be argued therefore, that the reaction of propene and molecular oxygen should have a similar rate
420 constant to the reaction toluene and molecular oxygen. Figure 5 compares $C_3H_6 + O_2$ [53–56] and
421 toluene + O_2 [58] rate constants.



422
423 Figure 5: $C_3H_6 + O_2$ rate constant comparison. — *This study* ($\pm 50\%$), — Goldsmith et al. [56],
424 - - - (Toluene+ O_2) Oehlschlaeger et al. [58], - · - Stothard and Walker [55].

425 The rate constant adopted in this study is estimated to best fit experimental data over a wide
426 range of conditions from the jet-stirred and flow reactors and shock tube. It is compared with rate
427 constants from the literature in Fig. 5. There is significant overlap over the temperature range
428 800–1200 K between the measured rate constant for toluene + O_2 from Oehlschlaeger et al. [58]
429 and the calculated rate constant from Goldsmith et al. for $C_3H_6 + O_2$ [56] above 1200 K.



(a) JSR: $\phi = 1.68, p = 1$ atm.

(b) Shock tube: $\phi = 1, p = 2$ and 10 atm (Mix 15 and

19 Part II [10]).

430 Figure 6: Effect of changing the $C_3H_6 + O_2$ rate constant on predicted JSR species profiles and
431 predicted shock tube ignition delay times. — *This study*, — Goldsmith et al. [56], - - -
432 (Toluene+O₂) Oehlschlaeger et al. [58], - · - Stothard and Walker [55].

434 Inclusion of the different rate constants results in reasonable agreement under JSR conditions
 435 as shown in Fig. 6(a). However, at high-pressure and relatively high-temperatures in the shock
 436 tube, Fig. 6(b), inclusion of the previous rate constant or the values from Stothard and Walker
 437 and Baulch et al. results in the under prediction of reactivity. The recommendation from
 438 Goldsmith et al. results in ignition delay time predictions that are slower than the measurements
 439 by approximately 20–30%, but this could be considered as reasonable agreement with the data.
 440 The rate constant for hydrogen atom abstraction by molecular oxygen from toluene from the
 441 study of Oehlschlaeger et al. also results in relatively good agreement with the ignition delay
 442 time data, but predicts ignition delay times that are approximately 20% faster than the
 443 measurements at 40 atm. The rate constant adopted in this study is estimated in order to best
 444 match experimental data, but we believe it requires further study.

445 3.2.7. $C_3H_6 + \dot{O} \leftrightarrow Products$

446 Rate constants for hydrogen atom abstraction by atomic oxygen are adopted from the review
 447 by Tsang [9]. These reactions did not show significant sensitivity during the course of this study.

448 Oxygen atom can also add to propene resulting in the formation of the following product sets:

- 449 • $C_3H_6 + \dot{O} \leftrightarrow \dot{C}_2H_5 + H\dot{C}O$
- 450 • $C_3H_6 + \dot{O} \leftrightarrow CH_2\dot{C}O + \dot{C}H_3 + \dot{H}$
- 451 • $C_3H_6 + \dot{O} \leftrightarrow CH_3CH\dot{C}O + \dot{H} + \dot{H}$

452 Oxygen atom addition reactions are chain branching reactions; they result in the formation of
 453 two or more radicals via the three pathways shown above. To our knowledge there is very little
 454 in the way of previous measurements or calculations of rate constants for these reactions in the
 455 literature. The recommendations in this study are estimated by analogy with the reactions of
 456 ethylene and atomic oxygen which are adopted from the study of Baulch et al. [16]. Savee et al.
 457 [60] studied the reaction of propene and atomic oxygen at 4 Torr and 298 K, and reported three
 458 bi-molecular product sets: $\dot{C}H_3 + \dot{C}H_2CHO$, $\dot{C}_2H_5 + H\dot{C}O$, and $H_2 + CH_3CH\dot{C}O$ similar to those
 459 mentioned above and the collisional stabilization products methyloxirane and propanal.
 460 Exclusion of the collisional stabilization products may be a possible reason the current
 461 mechanism under-predicts the propanal species profiles. We recommend further study of this
 462 reaction system under combustion relevant conditions.

463 3.3. $\dot{C}_3H_5 \leftrightarrow Products$

- 464 • $C_3H_{4-a} + \dot{H} \leftrightarrow \dot{C}_3H_{5-a}$
- 465 • $C_3H_{4-a} + \dot{H} \leftrightarrow C_3H_{4-p} + \dot{H}$
- 466 • $C_3H_{4-a} + \dot{H} \leftrightarrow C_2H_2 + \dot{C}H_3$
- 467 • $C_3H_{4-a} + \dot{H} \leftrightarrow \dot{C}_3H_{5-t}$
- 468 • $C_3H_{4-p} + \dot{H} \leftrightarrow \dot{C}_3H_{5-t}$
- 469 • $C_3H_{4-p} + \dot{H} \leftrightarrow \dot{C}_3H_{5-s}$
- 470 • $C_2H_2 + \dot{C}H_3 \leftrightarrow \dot{C}_3H_{5-s}$

471 \dot{C}_3H_{5-x} radicals (1-, 2-, 3-propenyl) can decompose to produce either allene and a \dot{H} atom or
 472 propyne and a \dot{H} atom. Other reactions that occur on the \dot{C}_3H_5 potential energy surface include the
 473 reaction of the C_3H_4 isomers and atomic hydrogen to form methyl radical and acetylene and the
 474 \dot{H} atom catalyzed isomerization reaction between allene and propyne. As observed during the
 475 course of this study, the \dot{C}_3H_{5-x} decomposition reactions only become competitive with the
 476 reactions of $\dot{C}_3H_{5-a} + HO_2$ and \dot{C}_3H_{5-s} or $\dot{C}_3H_{5-t} + O_2$ at a high temperatures. Miller et al. [61]

477 carried out an extensive study of the \dot{C}_3H_5 radical potential energy surface using RRKM theory
478 and master-equation calculations to determine the rate coefficients. The authors carried out an
479 extensive literature review of experimental and theoretical studies showing excellent agreement
480 between their results and the available experimental results. These rate constants have been
481 adopted in the current mechanism.

482 3.4. $\dot{C}_3H_5\text{-}a + \dot{R} \leftrightarrow \text{Products}$

483 3.4.1. $\dot{C}_3H_5\text{-}a + \dot{C}H_3 \leftrightarrow C_4H_8\text{-}1$

484 The recombination reaction of allyl and methyl radicals to give 1-butene is an important
485 inhibiting reaction for propene combustion, especially at lower temperatures, Figs. 1(b) and 18.
486 The current mechanism predicts that this reaction produces nearly all of the butene detected in
487 the JSR experiments. This chain terminating reaction acts to inhibit reactivity for ignition delay
488 time measurements. The rate constant included is from Tsang [9].

489 3.4.2. $\dot{C}_3H_5\text{-}a + H\dot{O}_2 \leftrightarrow \text{Products}$

490 The reactions of allyl and hydroperoxyl radicals are observed to be important across a range of
491 conditions, especially at low to intermediate temperatures, Figs. 1(a) and 18. At approximately
492 875 K and 1 atm in a JSR, the reaction of allyl and hydroperoxyl radicals accounts for
493 approximately half of all allyl radical consumption, Fig. 18. We have adopted the pressure
494 dependent rate constants for the bimolecular reactions of allyl radical with hydroperoxyl radical,
495 the thermal decomposition of allyl hydroperoxide (aC_3H_5OOH), and the unimolecular reactions
496 of allyloxy ($C_3H_5\dot{O}$) radical from the study of Goldsmith et al. [56]. It is the most recent and
497 comprehensive investigation of the allyl radical plus hydroperoxyl radical system.

498 $\dot{C}_3H_5\text{-}a + H\dot{O}_2$

- 499 • $\dot{C}_3H_5\text{-}a + H\dot{O}_2 \leftrightarrow C_3H_5\dot{O} + \dot{O}H$
- 500 • $\dot{C}_3H_5\text{-}a + H\dot{O}_2 \leftrightarrow aC_3H_5OOH$
- 501 • $\dot{C}_3H_5\text{-}a + H\dot{O}_2 \leftrightarrow C_2H_3CHO + H_2O$

502 aC_3H_5OOH

- 503 • $aC_3H_5OOH \leftrightarrow C_2H_3CHO + H_2O$
- 504 • $aC_3H_5OOH \leftrightarrow C_3H_5\dot{O} + \dot{O}H$

505 As shown in Fig. 7, at elevated temperatures and low-pressures, allyl radical reacts with
506 hydroperoxyl radical to form allyloxy and a hydroxyl radical. However, as temperatures decrease
507 and pressures increase the formation of the chemically activated adduct allyl hydroperoxide
508 becomes dominant. Allyl hydroperoxide subsequently decomposes to give allyloxy and hydroxyl
509 radicals.

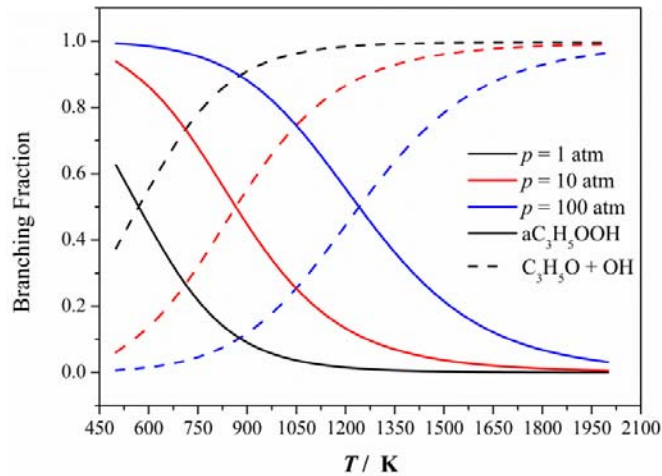
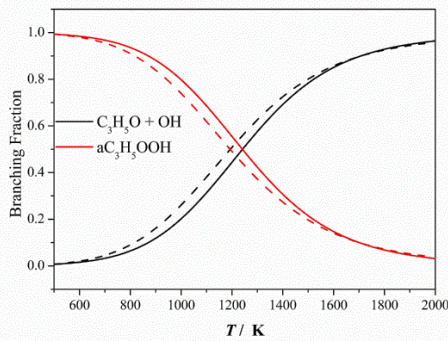
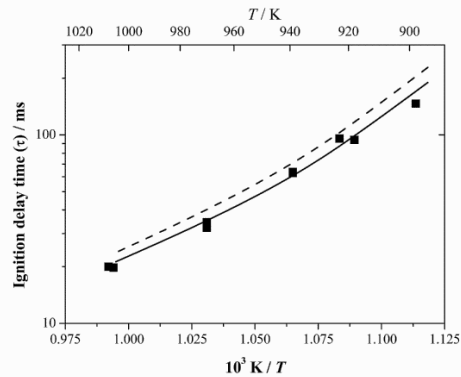


Figure 7: Branching ratio of $\dot{C}_3H_5\text{-a} + \dot{H}O_2 \leftrightarrow \text{Products}$.

510
511
512 The branching ratio for the $\dot{C}_3H_5\text{-a} + \dot{H}O_2$ reaction between the allyloxy producing channel
513 and the allyl hydroperoxide producing channel has been altered slightly from the
514 recommendation of Goldsmith et al. An additional 5% of the flux now proceeds via the allyl
515 hydroperoxide channel at the highest pressure, Fig. 8(a). This has resulted in better agreement
516 with RCM ignition delay time data, as shown in Fig. 8(b). At combustion relevant conditions
517 both of the major channels for the reaction of allyl radical and hydroperoxyl radical act to
518 promote reactivity as they ultimately convert a stable allyl radical to a reactive hydroxyl radical.



(a) Comparison of branching ratio at 100 atm.



(b) RCM: fuel/4% O_2 , $\phi = 1.0$ $p = 40$ atm.

519 Figure 8: Altering the $\dot{C}_3H_5\text{-a} + \dot{H}O_2$ branching ratio and its effect on predicted RCM ignition
520 delay times (Mix 11 [10]). — *This study*, - - - Goldsmith et al. [55].

521 $C_3H_5\dot{O} \leftrightarrow \text{Products}$

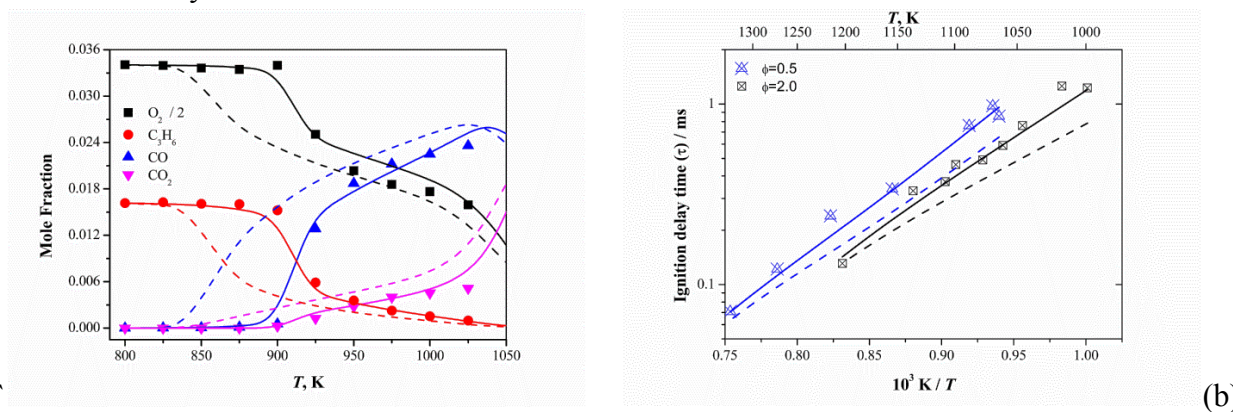
- 522 • $C_3H_5\dot{O} \leftrightarrow \dot{C}_2H_3 + CH_2O$
- 523 • $C_3H_5\dot{O} \leftrightarrow C_2H_3O\dot{C}H_2$
- 524 • $C_3H_5\dot{O} \leftrightarrow \dot{C}H_2CH_2CHO$
- 525 • $C_3H_5\dot{O} \leftrightarrow C_2H_3CHO + \dot{H}$
- 526 • $C_3H_5\dot{O} \leftrightarrow C_2H_4 + \dot{H}CO$

527 Allyloxy radical decomposes to give bi-molecular products such as vinyl radical and
528 formaldehyde, acrolein and atomic hydrogen, and ethylene and formyl radical. It can also
529 undergo isomerisation to give vinoxyl-methyl and formyl-ethyl radicals. The rate constants for

530 these reactions were also adopted from the study by Goldsmith et al. [56].

531 In AramcoMech 1.3, the reaction of allyl and hydroperoxyl radicals consisted of one channel
532 producing allyloxy radical ($C_3H_5\dot{O}$) and hydroxyl radicals via an estimated high-pressure limit
533 rate constant. Allyloxy radical was consumed via decomposition reactions or via $\dot{O}H$ addition to
534 form allyl hydroperoxide. Inclusion of the previous rate constants into the current kinetic scheme
535 results in a significant increase in reactivity as shown in Fig. 9.

536 Other rate constants in the allyl + HO_2 system which were not found to be competitive during
537 the course of this study but are incorporated into the mechanism from the study by Goldsmith et
538 al. [56] include $C_2H_3O\dot{C}H_2$ and $\dot{C}H_2CH_2CHO$ decomposition, and the reactions of vinyl radical
539 with formaldehyde.



(a) JSR: $\phi = 1.07$, $p = 1$ atm.

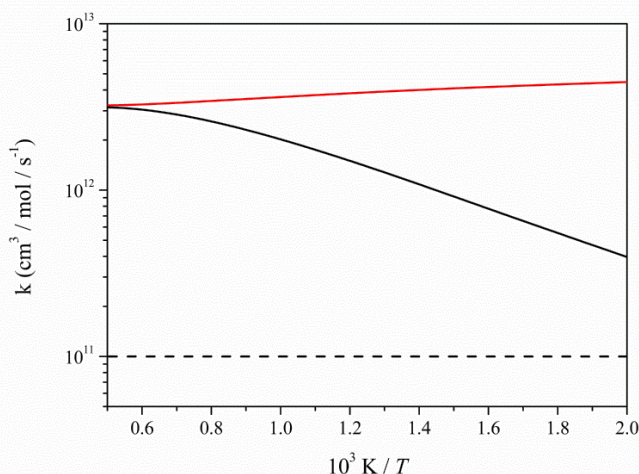
ST: $\phi = 0.5$ and 2.0 fuel/air, $p = 40$ atm.

540 Figure 9: Effect of using current — and previous [32] - - - \dot{C}_3H_5 -a + HO_2 rate constants on
541 predicted JSR species profiles and shock tube ignition delay times (Mix 27 and 30 [10]).

542 3.4.3. $\dot{C}_3H_5 + O_2 \leftrightarrow Products$

543 The reactions of allyl radical and molecular oxygen were not found to be particularly sensitive
544 during the course of this study. The reactions of allyl radical with hydroperoxyl radical or
545 recombination reactions are generally more competitive. The rate constants for the \dot{C}_3H_5 -a + O_2
546 reactions have been adopted from the study by Bozzelli and Dean [63].

547 To the best of our knowledge there have been no previous studies of the reactions of 2-
548 propenyl radical (\dot{C}_3H_5 -t) or 1-propenyl radical (\dot{C}_3H_5 -s) with molecular oxygen. During a recent
549 study of ethylene combustion, it was shown that the vinyl radical was consumed almost entirely
550 by reactions with molecular oxygen [32,34]. Similarly, the current mechanism predicts that under
551 JSR and flow reactor conditions \dot{C}_3H_5 -t and \dot{C}_3H_5 -s are almost exclusively consumed by reaction
552 with molecular oxygen, Figs. 18 and 26. The total rate constants for the reactions of both \dot{C}_3H_5 -t
553 and \dot{C}_3H_5 -s with molecular oxygen recommended in this study are estimated by analogy to the
554 reaction of vinyl radical and molecular oxygen from the high-level ab initio study by
555 Klippenstein et al. [64], Fig. 10. The authors stated that the predicted crossover temperature
556 between the aldehyde producing channel and the atomic oxygen producing channel occurs at a
557 temperature range of 1200–2500 K. The wide range is due to a 4 kcal/mol uncertainty in the
558 energy barrier to the transition state. Due to the importance of these reactions we recommend
559 further study of the total rate constants, the product channels, and the branching ratio between
560 these channels. The effect of including the updated rate constants is included in Fig. 12.



561
 562 Figure 10: Total rate constants for $\dot{C}_3H_5-t + O_2$ and $\dot{C}_3H_5-s + O_2$. — This study (analogy to \dot{C}_2H_3
 563 + O_2 [64]), — previous $\dot{C}_3H_5-t + O_2$, - - - previous $\dot{C}_3H_5-s + O_2$ recommendation [32].

564 $\dot{C}_3H_5-t + O_2 \leftrightarrow$ Products

- 565 • $\dot{C}_3H_5-t + O_2 \leftrightarrow CH_3CO\dot{C}H_2 + \ddot{O}$
 566 • $\dot{C}_3H_5-t + O_2 \leftrightarrow CH_3\dot{C}O + CH_2O$
 567 • $\dot{C}_3H_5-t + O_2 \leftrightarrow C_3H_4-a + H\dot{O}_2$

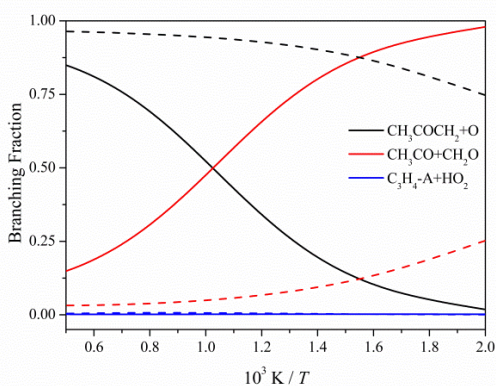
568 The \dot{C}_3H_5-t radical can react with molecular oxygen via three possible pathways. The acetyl
 569 radical and formaldehyde forming channel is chain propagating and inhibits reactivity, as it
 570 competes with a chain branching pathway that forms atomic oxygen and acetyl radical. The
 571 third pathway is a minor one and yields allene and a hydroperoxyl radical. In order to best match
 572 experimental measurements in the flow reactor and the RCM, the crossover temperature for the
 573 branching ratio between the chain branching channel ($CH_3CO\dot{C}H_2 + \ddot{O}$) and the propagating
 574 channel ($CH_3\dot{C}O + CH_2O$) has been reduced from 1200 K to 1000 K as recommended by
 575 Klippenstein et al. [64], Fig. 11.

576 In AramcoMech 1.3 the majority of the flux proceeded via the atomic oxygen producing
 577 channel at combustion relevant conditions and there was an over-prediction of reactivity,
 578 especially in the flow reactor. Sensitivity to the branching ratio between chain branching and
 579 chain propagating was observed at elevated pressures and relatively low temperatures, Fig. 1(a).

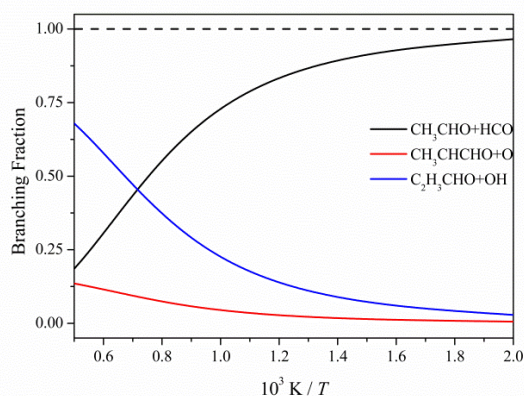
580 $\dot{C}_3H_5-s + O_2 \leftrightarrow$ Products

- 581 • $\dot{C}_3H_5-s + O_2 \leftrightarrow CH_3CHO + H\dot{C}O$
 582 • $\dot{C}_3H_5-s + O_2 \leftrightarrow C_2H_3CHO + \dot{O}H$
 583 • $\dot{C}_3H_5-s + O_2 \leftrightarrow CH_3\dot{C}HCHO + \ddot{O}$

584 The \dot{C}_3H_5-s radical also reacts with molecular oxygen via three possible pathways, Fig. 11.
 585 The acetaldehyde and formyl radical producing channel is the main source of acetaldehyde in the
 586 JSR as predicted by the current mechanism, Fig. 18. It is a chain propagating reaction and
 587 inhibits reactivity. The chain branching pathway results in the formation of $CH_3\dot{C}HCHO$ and $\dot{O}H$
 588 radicals while the minor channel forms acrolein and hydroxyl radical. The total rate constant for
 589 the reaction of \dot{C}_3H_5-s radical and molecular oxygen has also been estimated based on the
 590 reaction between vinyl and molecular oxygen from Klippenstein et al. [64].

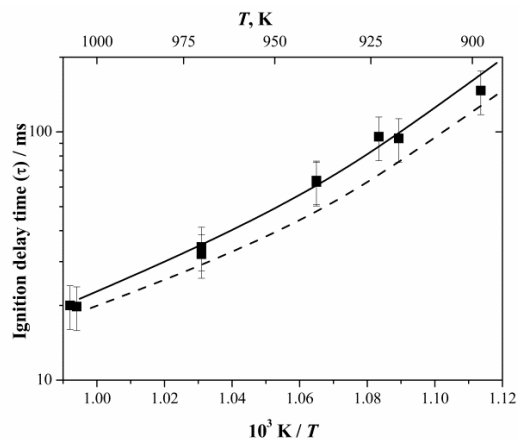


(a) $\dot{C}_3H_5\text{-t} + O_2$ branching ratio.

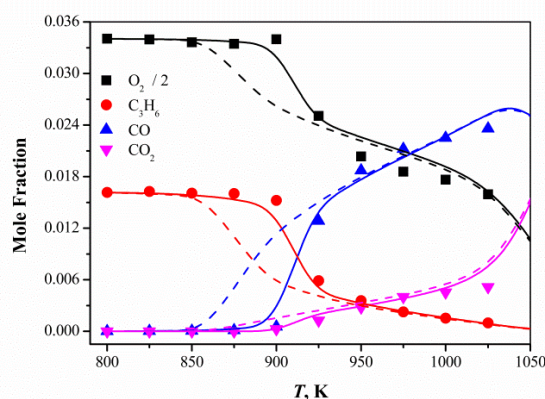


(b) $\dot{C}_3H_5\text{-s} + O_2$ branching ratio.

591 Figure 11: Branching ratios of the $\dot{C}_3H_5\text{-t} + O_2$ and $\dot{C}_3H_5\text{-s} + O_2$ reactions. — This study
 592 (analogy to $\dot{C}_2H_3 + O_2$ [64], - - - AramcoMech 1.3 [32].



(a) RCM: fuel/4% O_2 , $\phi = 1.0$, $p = 40$ atm.



(b) JSR: $\phi = 1.07$, $p = 1$ atm.

593 Figure 12: Effect of changing the $\dot{C}_3H_5\text{-s} + O_2$ and $\dot{C}_3H_5\text{-t} + O_2$ rate constants on predicted RCM
 594 ignition delay times (Mix 13 [10]) and JSR speciation measurements. — This study, - - -
 595 previous $\dot{C}_3H_5\text{-s}$ and $\dot{C}_3H_5\text{-t} + O_2$ [32].

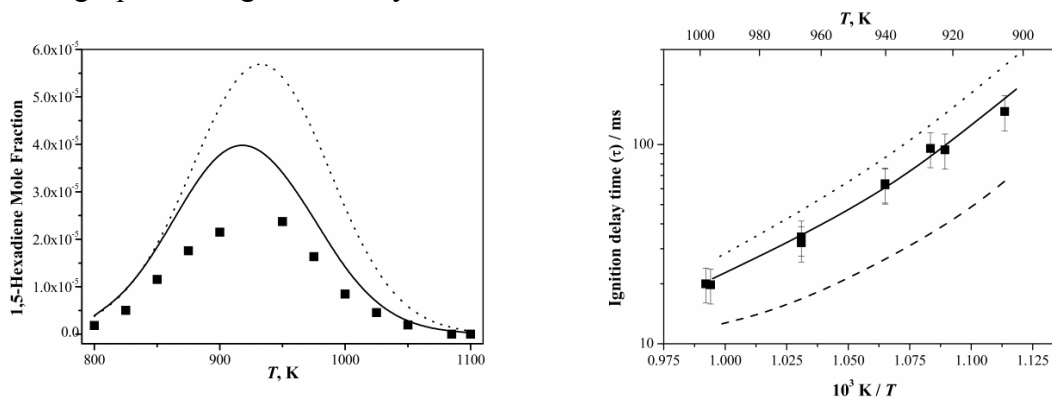
596 3.5. 1,5- C_6H_{10}

597 3.5.1. $C_6H_{10} \leftrightarrow \dot{C}_3H_5\text{-a} + \dot{C}_3H_5\text{-a}$

- 598 • $\dot{C}_3H_5\text{-a} + \dot{C}_3H_5\text{-a} \leftrightarrow C_6H_{10}$
- 599 • $\dot{C}_3H_5\text{-a} + \dot{C}_3H_5\text{-a} \leftrightarrow C_3H_4\text{-a} + C_3H_6$

600 Allyl radicals can undergo self-recombination to form 1,5-hexadiene. This chain terminating
 601 reaction inhibits reactivity at low and intermediate temperatures. Allyl radical self-reaction can
 602 also result in the formation of allene and propene. However, this channel accounts for less than
 603 5% of the total flux.

604 AramcoMech 1.3 did not include the allyl-allyl self-reaction, however, as significant amounts
 605 of 1,5-hexadiene were detected in the JSR it was necessary to include a rate constant for this
 606 reaction. In this study we have adopted a rate constant for allyl radical self-reaction based on the
 607 recommendations of two recent papers by Tranter and co-workers [65, 66]. The decomposition of
 608 1,5-hexadiene was investigated experimentally in a shock-tube [65] and theoretically with a
 609 Gorin-type RRKM calculation [66]. However, the rate constant adopted in this study is 30% less
 610 that of Lynch et al. [65]. This reduction is within the stated uncertainty and was required to
 611 match the high-pressure ignition delay time measurements.



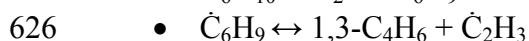
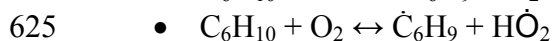
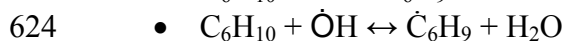
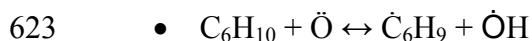
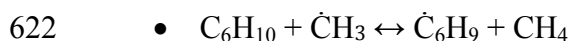
(a) JSR: $\phi = 2.19$, $p = 1$ atm.

(b) RCM: $\phi = 1.0$, 4% O_2 , $p = 40$ atm.

612 Figure 13: Effect of including the $\dot{C}_3H_5\text{-a} + \dot{C}_3H_5\text{-a} \leftrightarrow C_6H_{10}$ rate constant on predicted JSR
 613 species profiles and RCM ignition delay times (Mix 13 [10]). — This study, - - - excluding allyl
 614 recombination, ··· previous C_6H_{10} thermochemistry.

615 Tranter and co-workers highlighted the importance of 1,5-hexadiene thermochemistry in their
 616 study [65]. We have adopted their recommendation for the heat of formation and molar entropy.
 617 Figure 13 highlights the effect of thermochemistry. At 800 K using the standard molar entropy
 618 value from Lynch et al. results in a reduction of approximately a factor of two in the rate constant
 619 for the formation of 1,5-hexadiene.

620 3.5.2. C_6H_{10} sub-mechanism



627 The rate constants for hydrogen atom abstraction from 1,5-hexadiene by radical species have
 628 been adopted from the work of Orme and coworkers [67, 68]. Rate constants for other reactions
 629 such as hydrogen atom abstraction by molecular oxygen have been estimated based on their BDE
 630 and the number of hydrogen atoms available for abstraction as described by Ingham et al. [69].

631 These reactions were not found to be sensitive for propene oxidation. The resulting \dot{C}_6H_9 radical
632 decomposes to form 1,3-butadiene and a vinyl radical.

633 3.6. *Allene/propyne sub-mechanism*

634 Previously [32], rate constants for the allene/propyne sub-mechanism were adopted from
635 various sources [41, 70, 71]. Hansen et al. [72] recently published a mechanism for the
636 combustion of allene and propyne in flames. They reported rate constants for fuel consumption,
637 allene and propyne isomerisation, reaction of propargyl radical with molecular oxygen, and of
638 isomer specific formation of C_6 aromatic species. We have adopted the Hansen et al. [72] sub-
639 mechanism in the current kinetic scheme. For reactions that were not featured in the Hansen et al.
640 study, such as hydrogen atom abstraction by molecular oxygen from both C_3H_4 isomers, rate
641 constants have been estimated based on the bond dissociation energy (BDE) for the activation
642 energy and the number of hydrogen atoms available for abstraction for the A-factor as described
643 by Ingham et al. [69].

644 Hydroxyl radical addition rate constants are estimates [73, 74] while rate constants for
645 abstraction by $\dot{O}H$ are described as analogous to reactions involving C_3H_6 . Rate constants for
646 propargyl and hydroperoxyl radical reactions are included using analogies to the reactions of
647 allyl radical and $H\dot{O}_2$, which were adopted from Goldsmith et al. [75]. Further details of the C_3H_4
648 isomer sub-mechanism are included in the PhD thesis of Burke [76], which describes validation
649 of the allene/propyne mechanism against speciation measurements in a JSR and ignition delay
650 measurements in a shock tube.

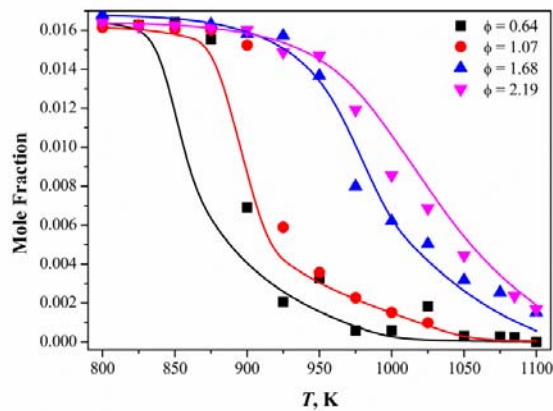
651 4. Results and discussion

652 4.1. *Jet-stirred reactor results*

653 Concentration profiles of stable species measured during the experiments have been simulated
654 using the kinetic model developed during this study. Experimental measurements were obtained
655 at four equivalence ratios, $\phi = 0.64, 1.07, 1.68$ and 2.19 , over a temperature range of 800 – 1100 K
656 and at near-atmospheric pressure. Figures 14–17 shows the performance of the current
657 mechanism and the current mechanism compared with the performance of AramcoMech 1.3
658 [32], in Fig. 19. Overall there is good agreement between the current mechanism and the
659 experimental measurements. The biggest discrepancy in its performance is the consistent under-
660 prediction of benzene and propanal.

661 4.1.1. *Mechanism performance*

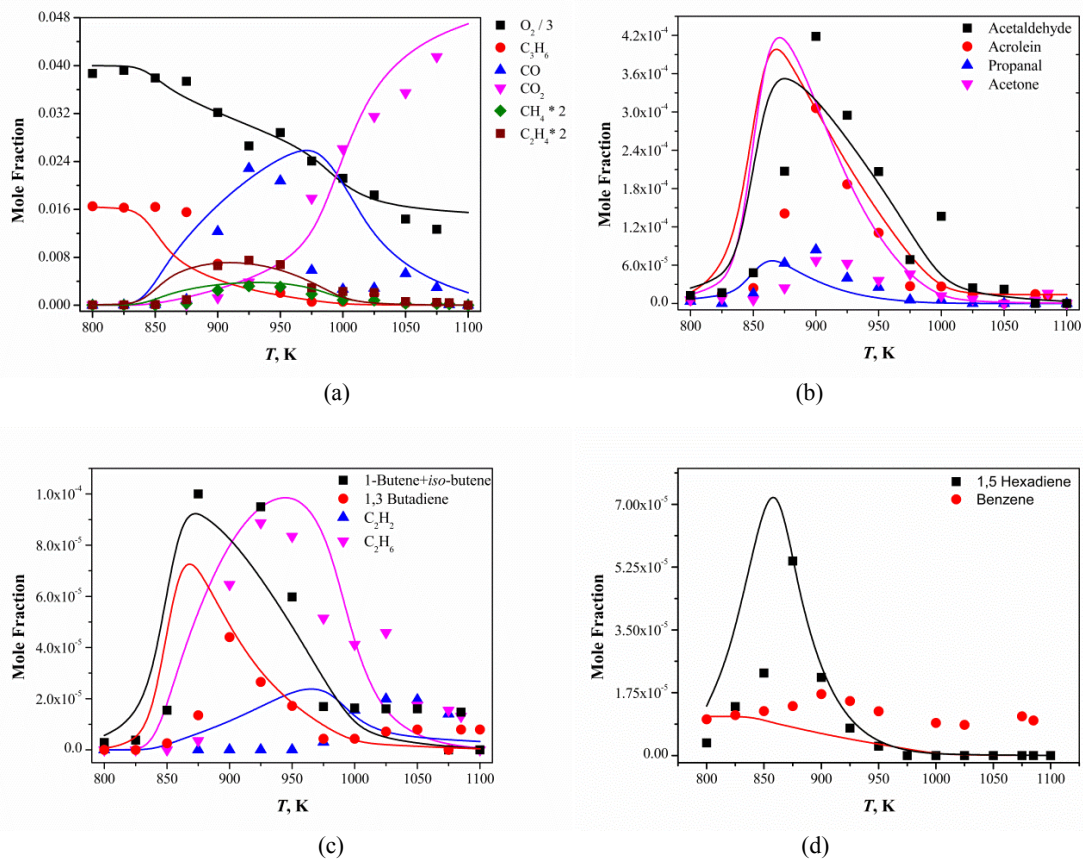
662 Figures 14–17 show the current mechanism performance against the experimental
663 measurements with general good agreement between both. Figure 14 shows that reactivity
664 decreases as equivalence ratio increases, and the current mechanism accurately predicts this
665 effect.



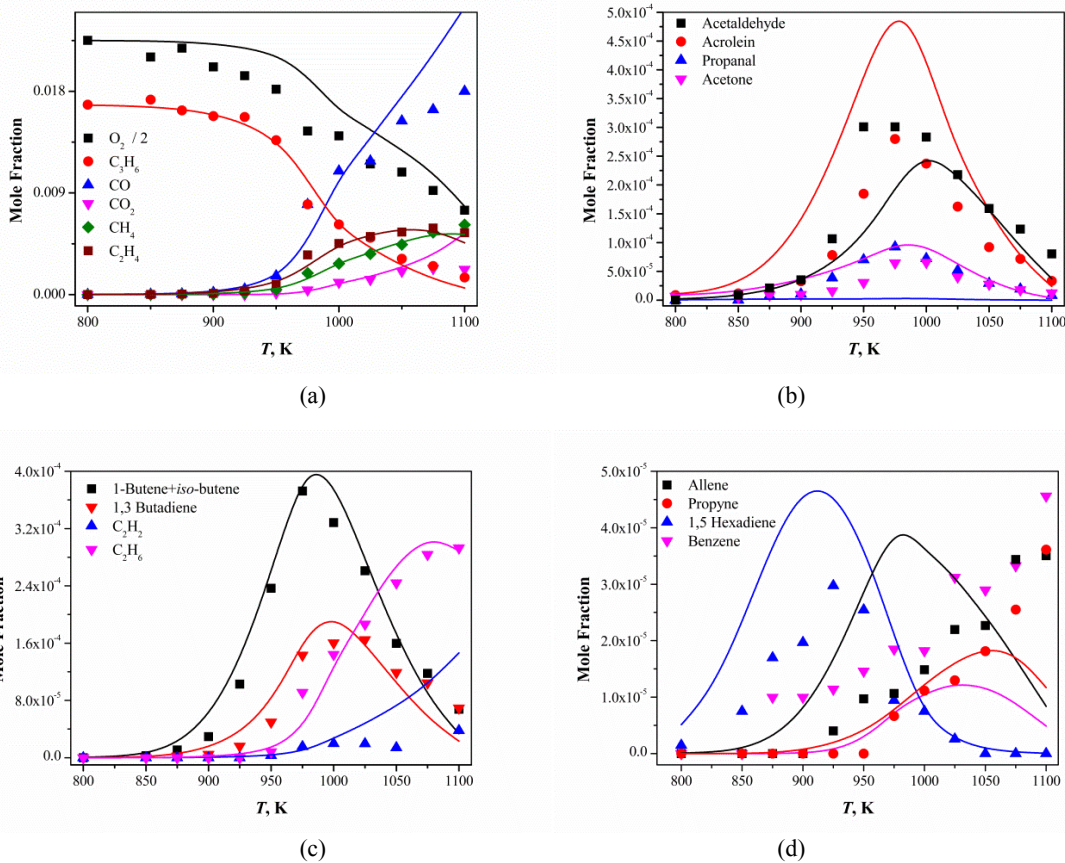
666
667 Figure 14: Comparison of $\approx 1.65\%$ C_3H_6 consumption at varying equivalence ratios, $p = 1.05$
668 atm, $\tau = 2.0$ s. Symbols: JSR experimental measurements, lines: current mechanism predictions.

669 To determine the important pathways controlling propene combustion under fuel-rich
670 conditions a flux analysis was carried out and is presented Fig. 18.

671 Hydrogen atom abstraction reactions from propene are important under all conditions in the
672 JSR. Hydrogen atom addition reactions to propene resulting in the formation of stable species
673 such as ethylene and methyl oxirane and methyl, ethyl formyl and iso-propyl radical species were
674 also highlighted as fuel consumption pathways. Propene decomposition reactions were not
675 observed as consumptions pathways under the conditions of this study in the JSR.



676
677
678
679
680 Figure 15: 1.65% C_3H_6 , 11.60% O_2 in He, $\phi = 0.64$, $p = 1.05$ atm, $\tau = 2.0$ s. Symbols: JSR
681 experimental measurements, lines: current mechanism predictions.

683
684685
686

687 Figure 16: 1.68% C_3H_6 , 4.0% O_2 in He, $\phi = 1.68$, $p = 1.05$ atm, $\tau = 2.0$ s. Symbols: JSR
688 experimental measurements, lines: current mechanism predictions.

689 4.1.2. Flux analysis for $\phi = 2.19$ in the JSR

690 The mechanism can accurately predict the oxidation of propene in a JSR under fuel-rich
691 conditions, predicting consumption of the fuel and oxygen and the formation of major
692 intermediate and product species correctly. Figure 18 shows a flux analysis at 970 K for the fuel-
693 rich mixture in Fig. 17. At this temperature 20% of the fuel has been consumed

694 4.1.3.

695 consumption

 C_3H_6

696 The main consumption pathways for propene include:

- 697 1. Hydrogen atom abstraction to form \dot{C}_3H_5 -a, \dot{C}_3H_5 -t and \dot{C}_3H_5 -s radicals.
- 698 2. Hydrogen atom addition reactions to form $i\text{-}\dot{C}_3H_7$ radical and $C_2H_4 + \dot{C}H_3$.
- 699 3. Hydroxyl radical addition to form \dot{C}_3H_6OH radicals.
- 700 4. Hydroperoxyl radical addition to form methyl oxirane.

701 Radicals such as hydroxyl, hydroperoxyl, methyl, and atomic oxygen all abstract atomic
702 hydrogen from propene. Under the conditions presented in Fig. 17, almost half of the propene
703 consumed propene is converted to allyl radical via hydrogen atom abstraction and also results in
704 the formation of the \dot{C}_3H_5 -t (4%) and \dot{C}_3H_5 -s (5 %).

705 Approximately 26% of propene is consumed via reactions by hydrogen atom addition

706 resulting in the formation of ethylene and methyl radical or iso-propyl radical. Other
707 consumption channels include the addition reactions with hydroperoxyl radical yielding methyl-
708 oxirane ($C_3H_6O_{1-2}$) and hydroxyl radicals forming $\dot{C}_3H_6OH_{2-1}$ radical.

709 4.1.4. \dot{C}_3H_5 -a consumption

710 The main consumption pathways for allyl radical include:

- 711 1. Reaction with hydroperoxyl radical to form $C_3H_5\dot{O}$, and aC_3H_5OOH .
- 712 2. Recombination reaction with methyl radical to form C_4H_8 -1.
- 713 3. Reaction with molecular oxygen to form vinoxy radical and formaldehyde or
714 acrolein and hydroxyl radical.
- 715 4. Recombination reaction with itself to form C_6H_{10} 1-5.

716 Over 45% of the allyl radicals formed react with hydroperoxyl radicals. This can result in the
717 formation of allyloxy radicals ($C_3H_5\dot{O}$) and hydroxyl radicals (44%) or can result in the
718 formation of allyl hydroperoxide (aC_3H_5OOH) (2.6%) which subsequently decomposes to form
719 allyloxy and hydroxyl radicals. Allyloxy radical undergoes an isomerization reactions to form
720 formyl-ethyl radical ($\dot{C}H_2CH_2CHO$) or vinoxyl-methyl radicals ($C_2H_3O\dot{C}H_2$) or can decompose
721 to give acrolein and atomic hydrogen or ethylene and a formyl radical. In addition to reactions
722 with HO_2 , allyl radical can undergo radical-radical recombination reactions with itself or with
723 methyl radicals to produce 1,5-hexadiene (6.8%) or 1-butene (24.8%) respectively. The
724 mechanism predicts that these recombination reactions are the main source of both C_6H_{10} and
725 C_4H_8 detected in the JSR. Allyl radical can also undergo reactions with molecular oxygen to
726 form vinoxy radical and formaldehyde or acrolein and hydroxyl radical or can decompose to
727 form allene and atomic hydrogen.

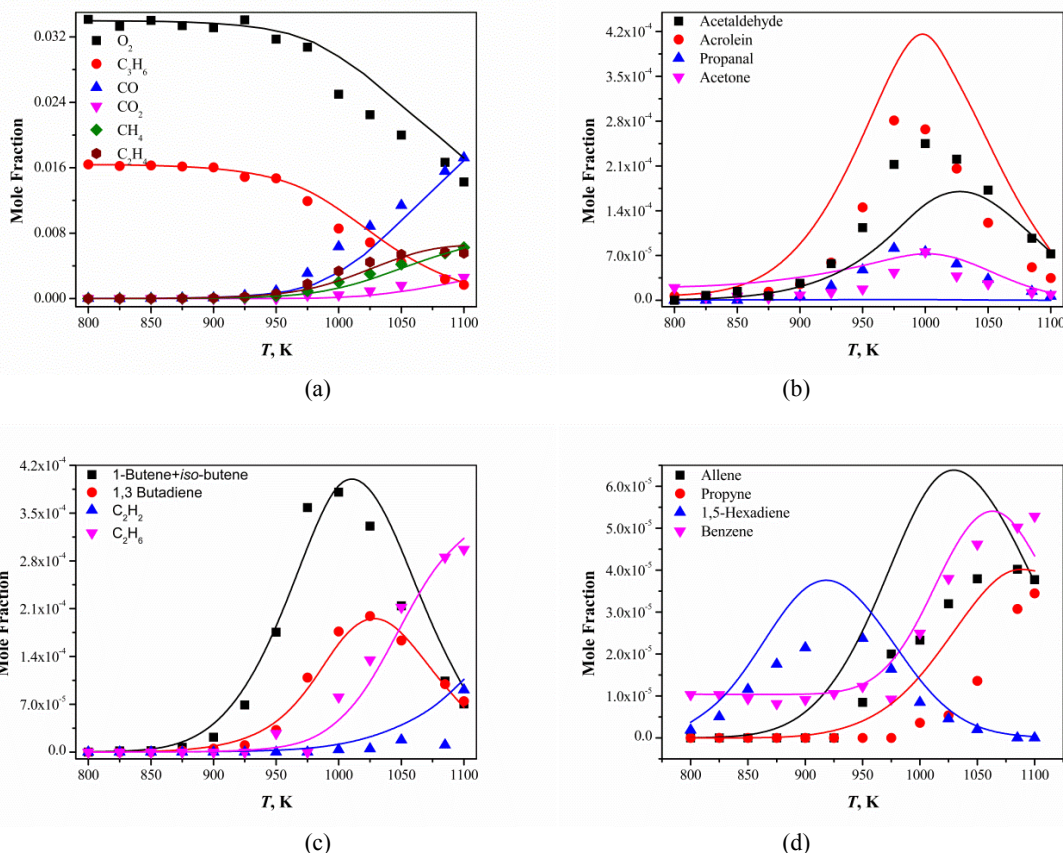
728 4.1.5. \dot{C}_3H_5 -s and \dot{C}_3H_5 -t consumption

729 The other \dot{C}_3H_5 radicals, 2-propenyl (\dot{C}_3H_5 -t) and 1-propenyl (\dot{C}_3H_5 -s), mainly react with
730 molecular oxygen. \dot{C}_3H_5 -t + O_2 resulting in the formation of formaldehyde and acetyl radical
731 (49.7%) or atomic oxygen and acetyl radical (48.7%). The reaction of \dot{C}_3H_5 -s + O_2 forms
732 acetaldehyde and formyl radical (61.2%), acrolein and hydroxyl radical (16.8%), or $CH_3\dot{C}HCHO$
733 radical and atomic oxygen (3.4%). The reaction of 1-propenyl radical and molecular oxygen is
734 predicted to be the main source of acetaldehyde in the JSR. The decomposition of \dot{C}_3H_5 -s to
735 acetylene and methyl radical accounts for almost 18% of 1-propenyl radical consumption and is
736 predicted to be the main source of acetylene in the JSR.

737 4.1.6. Mechanism performance

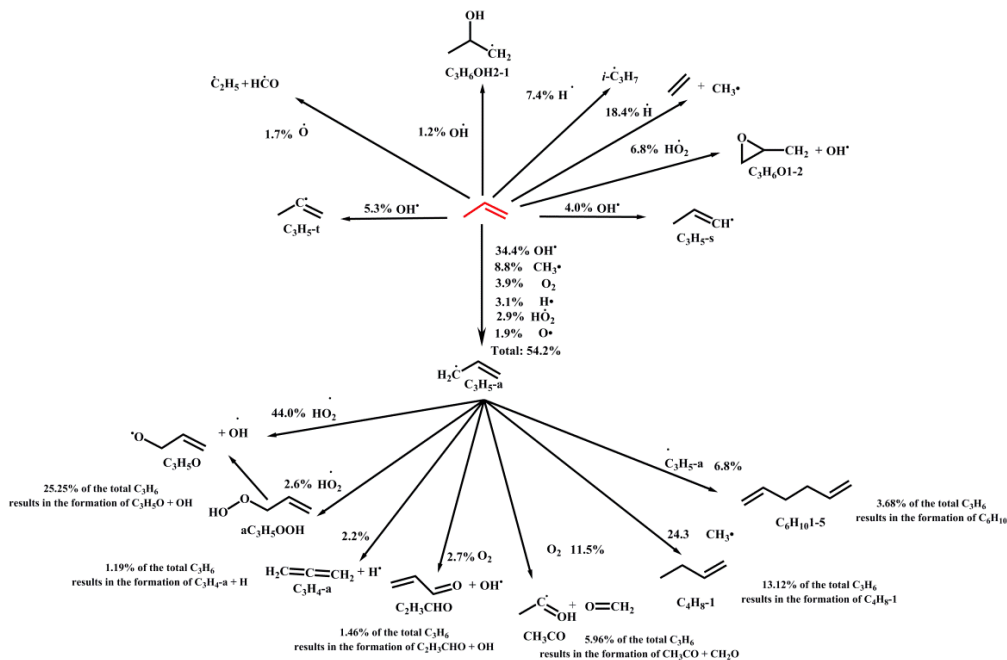
738 Figures 15, 16 and 19 show species profiles for propene oxidation in a JSR at $\phi = 0.64$, 1.68,
739 and 1.07 respectively. The experimental measurements are compared to predictions from the
740 current mechanism, which is able to predict the profiles for fuel and oxygen consumption and
741 also predicts the main intermediate and product species profiles. The mechanism over predicts
742 the concentration of acetylene across the range of equivalence ratios. Approximately 20 ppm of
743 acetylene is formed in the JSR at $\phi = 1.68$ at 1000 K, but the mechanism predicts approximately
744 50 ppm. The mechanism consistently under-predicts the concentrations of benzene at $\phi \leq 1.68$,
745 and propanal at $\phi = 1.07$ –2.19. Currently, the reason behind the under-prediction of benzene
746 yields is unknown. The propargyl radical formed does not undergo recombination to form
747 benzene but reacts with molecular oxygen. Under fuel-rich conditions as shown in Fig. 17
748 benzene is formed via the \dot{C}_3H_5 -a + $\dot{C}_3H_3 \rightarrow C_6H_6 + \dot{H} + \dot{H}$ reaction, however this is not a dominant
749 reaction pathway under fuel-lean conditions. The causes of the under-prediction of propanal is
750 also unclear. In general propanal comes from $\dot{C}_3H_6OH_{1-2} + O_2 \leftrightarrow C_2H_5CHO + HO_2$ and

751 $C_2H_5CHO + \dot{H} \leftrightarrow \dot{C}_3H_6OH1-2$ and acetone comes from the reactions $CH_3COCH_3 + \dot{H} \leftrightarrow \dot{C}_3H_6OH2-1$
 752 and $\dot{C}_3H_6OH2-1 + O_2 \leftrightarrow CH_3COCH_3 + \dot{HO}_2$. The \dot{C}_3H_6OH radicals are formed via \dot{OH} addition to
 753 C_3H_6 . These rate constants were adopted from Zádor et al. [47]. Their recommendation of a
 754 50:50 ratio of terminal to central addition has been altered to a 75:25 ratio in order to reduce the
 755 over-prediction of acetone and under-prediction of propanal. As shown in Figs. 16, 17 and 19
 756 this alteration was not sufficient. Further alteration of the current 75:25 ratio is not supported in
 757 the current literature. Acrolein is over-predicted at $\phi = 1.68$ and 2.19. Acrolein is almost
 758 exclusively produced from the $\dot{C}_3H_5-a + \dot{HO}_2$ system all of the rate constants for these reactions
 759 have been adopted from the study of Goldsmith et al.[56]. At this time we are unsure of the
 760 causes of the over-prediction under fuel-rich conditions.



763
764
765 Figure 17: 1.64% C_3H_6 , 3.38% O_2 in He, $\phi = 2.19$, $p = 1.05$ atm, $\tau = 2.0$ s. Symbols: JSR
766 experimental measurements, lines: current mechanism predictions.

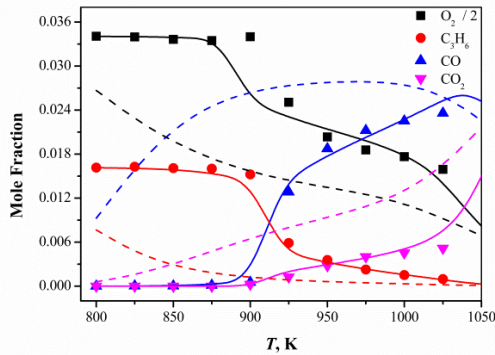
767 There is good agreement between the experimental measurements and the current mechanism
 768 at $\phi = 2.19$. As shown in Fig. 14, reactivity decreases going from fuel-lean to fuel-rich mixtures.
 769 After 2.0 s, approximately 20% of the propene consumption occurs at 1000 K for the $\phi = 2.19$
 770 mixture, while 20% consumption occurs at approximately 875 K for the $\phi = 0.64$ mixture. The
 771 mechanism can accurately predict this shift in reactivity as a function of equivalence ratio. The
 772 mechanism predicts an increased influence of chain terminating reactions, thereby reducing the
 773 overall reactivity under fuel-rich conditions.
 774



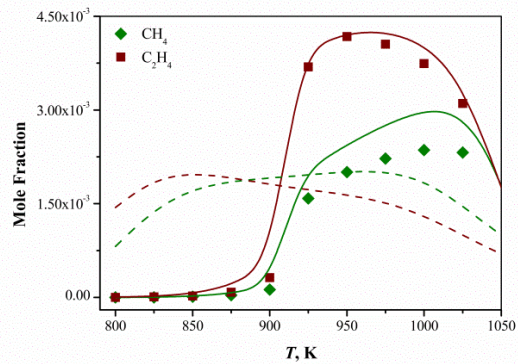
775 Figure 18: Flux analysis for the oxidation of a mixture of 1.67% C₃H₆, 3.38% O₂ diluted in
 776 helium, $\phi = 2.19$ at 970 K.

777 4.1.7. Comparison with the previous mechanism's performance

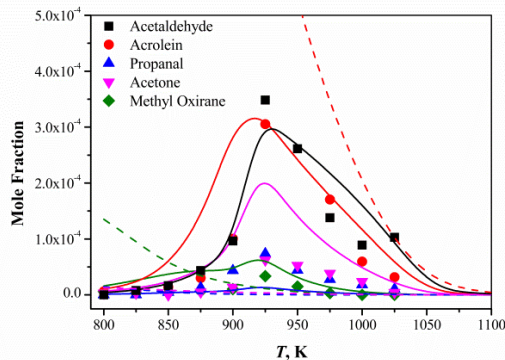
778 Figure 19 shows the results of the improved chemical kinetic scheme in comparison with the
 779 performance of AramcoMech 1.3 against the experimental measurements at $\phi = 1.07$. The
 780 previous mechanism over-predicted reactivity and predicted reactivity at a significantly lower
 781 temperature than the current mechanism. At 800 K, the current mechanism predicts < 1% fuel
 782 consumption while the previous mechanism predicts 53% consumption. The current mechanism
 783 can accurately predict the profiles of many of the intermediate species, such as methane,
 784 ethylene, acetaldehyde, acrolein, butene, 1,3-butadiene, and 1,5-hexadiene, while AramcoMech
 785 1.3 could not. The changes from the previous to the current mechanism that had the largest effect
 786 on the mechanism performance in the JSR include: the updated rate constants for C₃H₆ + OH, the
 787 inclusion of rate constants for C₃H₅-a+HO₂ system, and C₃H₅-a+C₃H₅-a recombination.



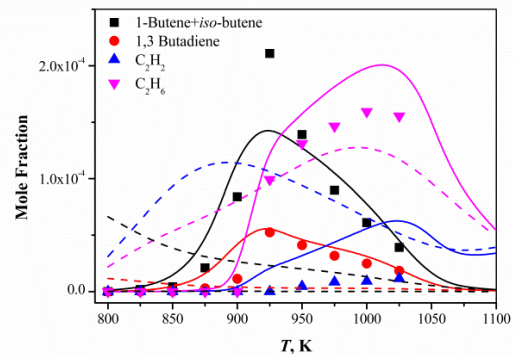
(a)



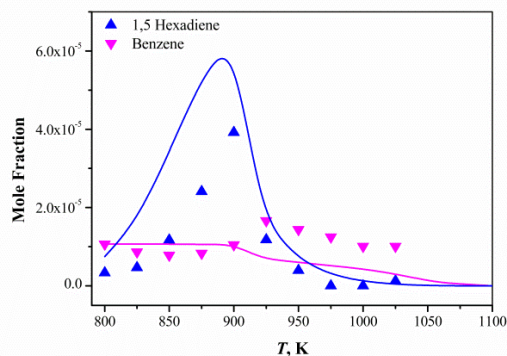
(b)



(c)



(d)



(e)

789

790

791

792

793

794

795 Figure 19: 1.62% C_3H_6 , 6.81% O_2 in He, $\phi = 1.07$, $p = 1.05$ atm, $\tau = 2.0$ s. Symbols: JSR
796 experimental measurements, lines: — current mechanism, - - - AracmoMech 1.3 [31].

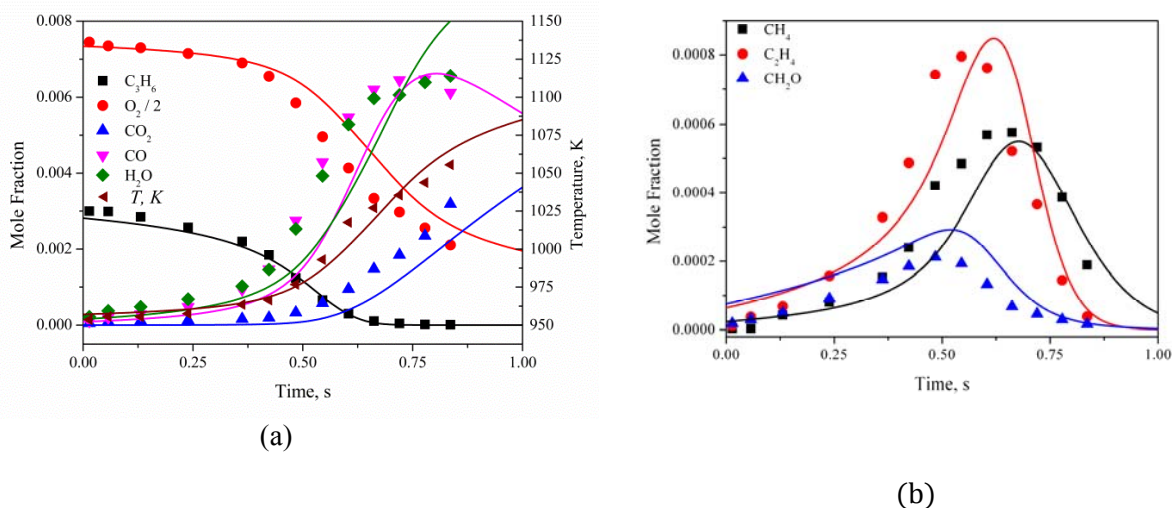
797 4.2. Flow reactor results

798 Experiments for propene oxidation have been performed at Princeton University in two flow
799 reactors: the Variable Pressure Flow Reactor (VPFR) and the High Pressure Laminar Flow
800 Reactor (HPLFR). Experiments were conducted at elevated pressures, low and intermediate
801 temperatures, over a range of equivalence ratios as a function of residence time.

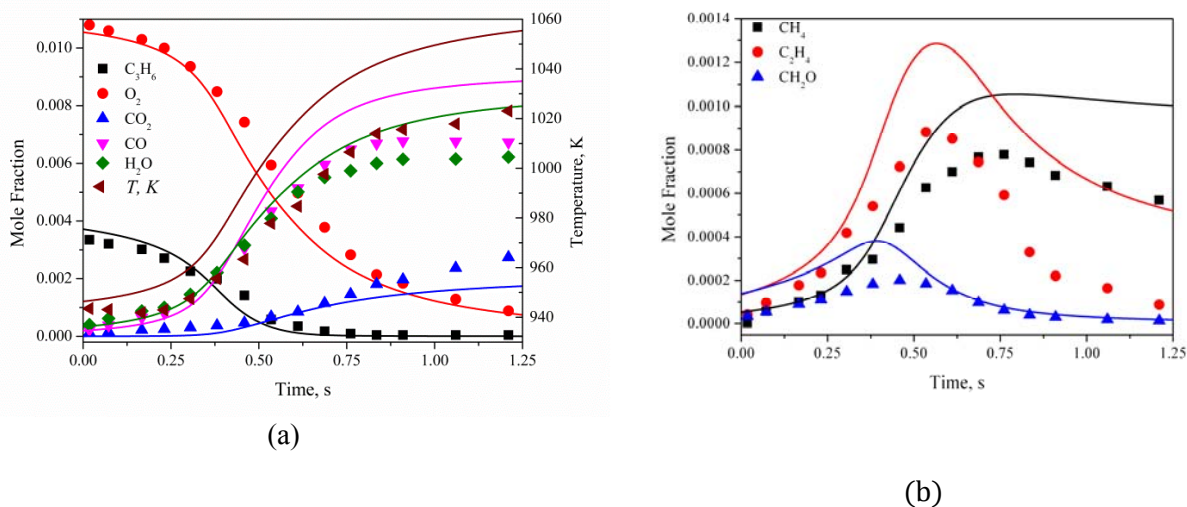
802 4.2.1. Variable Pressure Flow Reactor (VPFR)

803 Propene oxidation was studied experimentally in the VPFR over a pressure range of 8–12.5
804 atm and in the temperature range 612–1047 K. The VPFR can be simulated using a constant

805 pressure adiabatic assumption and relative time shift between simulation and experimental time
 806 [27]. In this study the mechanism is shifted to match approximately 50% fuel consumption.
 807 There is good agreement between the mechanism and the experimental measurements across the
 808 range of pressures, temperatures, and equivalence ratios, Figs. 20 and 21. Additional plots for
 809 other experimental conditions are included in the Supplementary Material.



810 Figure 20: 0.31% C₃H₆, 1.149% O₂ in N₂, $\phi = 0.94$, $p = 8$ atm, $T = 955$ K. Symbols: VPFR
 811 experimental measurements, lines: current mechanism predictions, time shift: -0.38 s.

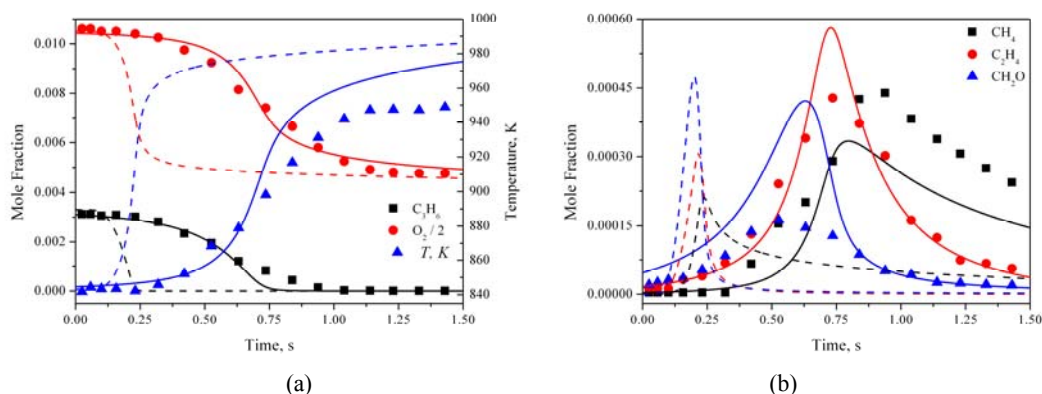


812 Figure 21: 0.34% C₃H₆, 1.1% O₂ in N₂, $\phi = 1.37$, $p = 10$ atm, $T = 942$ K. Symbols: VPFR
 813 experimental measurements, lines: current mechanism predictions, time shift: -0.62 s.

814 4.2.2. Previous mechanism performance

815 A comparison of the performance of the current mechanism and AramcoMech 1.3 [32] is
 816 shown in Fig. 22. The conditions in this example are: $\phi = 0.70$ mixture at a pressure of 12.5 atm
 817 and initial reaction temperature of 843 K. Unlike the predictions of the current mechanism, the
 818 simulations for the previous mechanism could not be meaningfully time shifted to agree with the

819 experimental measurements; for this reason the AramcoMech 1.3 predictions are not time
 820 shifted. The required positive time shift for the AramcoMech 1.3 predictions (relative to the
 821 experimental timeframe) is contrary to the physics of the preheated, non-premixed VPFR
 822 reacting flowfield, which tends to reduce chemical induction times relative to idealized reacting
 823 plug flow conditions. This reduced induction time amounts to a negative time shift from ideal
 824 time zero, which should be qualitatively matched by a negative time shift for modeling
 825 predictions. See ref. [27] for further discussion of this issue.



826
827

828 Figure 22: 0.33% C_3H_6 , 2.10% O_2 in N_2 , $\phi = 0.70$, $p = 12.5$ atm, $T = 843$ K. Symbols: VPFR
 829 experimental measurements, Lines: — current mechanism (time shift: -0.75 s), - - -
 830 AramcoMech 1.3 [32] (no time shift).

831 In comparison to AramcoMech 1.3, in the current mechanism less of the allyl radical is
 832 consumed by reaction with hydroperoxyl radical and more is consumed via chain terminating
 833 reactions such as self-recombination to form 1,5-hexadiene. Therefore the current mechanism is
 834 less reactive compared to AramcoMech 1.3.

835 4.2.3. High Pressure Laminar Flow Reactor (HPLFR)

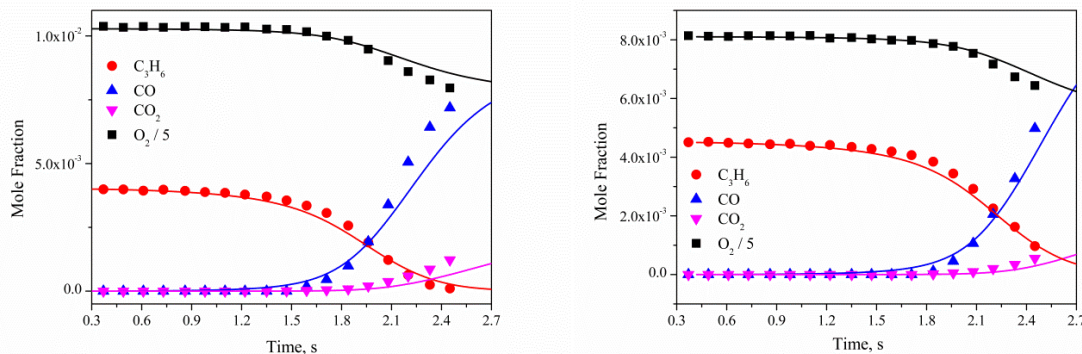
836 Propene oxidation experiments conducted in the HPLFR were at a fixed pressure of 15.0 ± 0.1
 837 atm. For each of the four HPLFR experiments reported here, the measured axial temperature
 838 profile of the flow prior to addition of oxidizer was a constant 800 ± 5 K along the test section.
 839 Upon addition of O_2 to the C_3H_6/N_2 mixture, the measured temperature increase from the 800 K
 840 baseline was less than $+20$ K for fuel-lean experiments, and less than $+5$ K for the stoichiometric
 841 and fuel-rich cases. For this reason the experiments are defined as near-isothermal. Initial fuel
 842 mole fractions ranged from 4000 to 6250 ppm for equivalence ratios of $\phi = 0.35$, 0.5, 1.0, and
 843 1.25. These experiments have been simulated using an isothermal assumption. The mechanism
 844 was time shifted in order to best match the propene concentration at fuel-lean conditions, (Fig.
 845 23), and to match the water concentration for the stoichiometric and fuel-rich conditions, (Figs.
 846 24 and 25), since the measured water profile has the highest gradient relative to its measurement
 847 uncertainty (i.e., it is the most sensitive measurement).

848 In addition to the species reported in Figs. 23–25, the gas chromatograph (GC) was calibrated
 849 to measure H_2 , CH_4 , C_2H_6 , allene, and propyne but the mole fractions of these species were
 850 below detection/quantification limits of the experiments. Water and formaldehyde profiles have
 851 been omitted from the fuel-lean measurements due to sample condensation observed during the
 852 experiments.

854 4.2.4. Mechanism performance

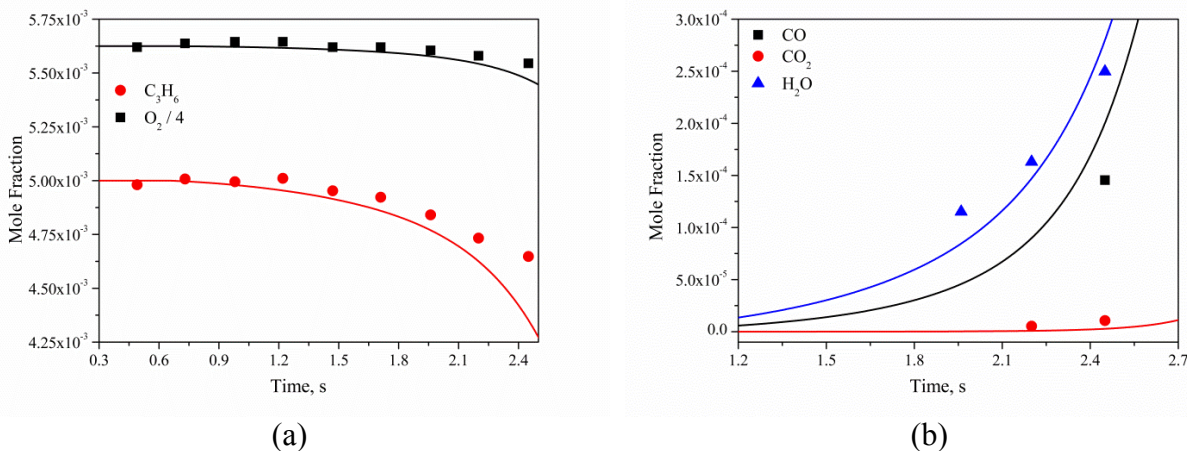
855 Overall there is good agreement between the mechanism predictions and the HPLFR
 856 experimental measurements. The stoichiometric and fuel-rich mixtures show very little
 857 reactivity, Figs. 24 and 25 respectively. Less than 7% of the fuel is consumed by the end of the
 858 experiment for the stoichiometric mixture, Fig. 24, and less than 8% is consumed in the $\phi = 1.5$
 859 mixture, Fig. 25.

860 A flux analysis for a $\phi = 0.35$ at 1.3 s mixture is included in Fig. 26, at 1.3 s 20% fuel has
 861 been consumed. It serves to highlight the important pathways controlling propene oxidation under
 862 the conditions studied in the HPLFR and gives an overview of propene combustion and the
 863 pathways that form intermediate and product species.

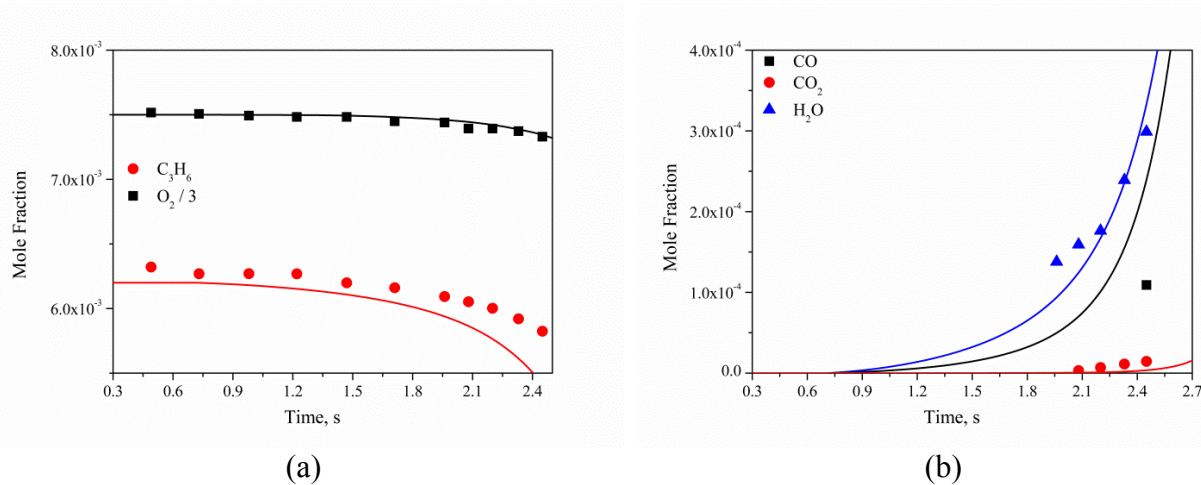


864 (a) 0.40% C₃H₆, 5.14% O₂ in N₂, $\phi = 0.35$ (b) 0.45% C₃H₆, 4.05% O₂ in N₂, $\phi = 0.5$
 865

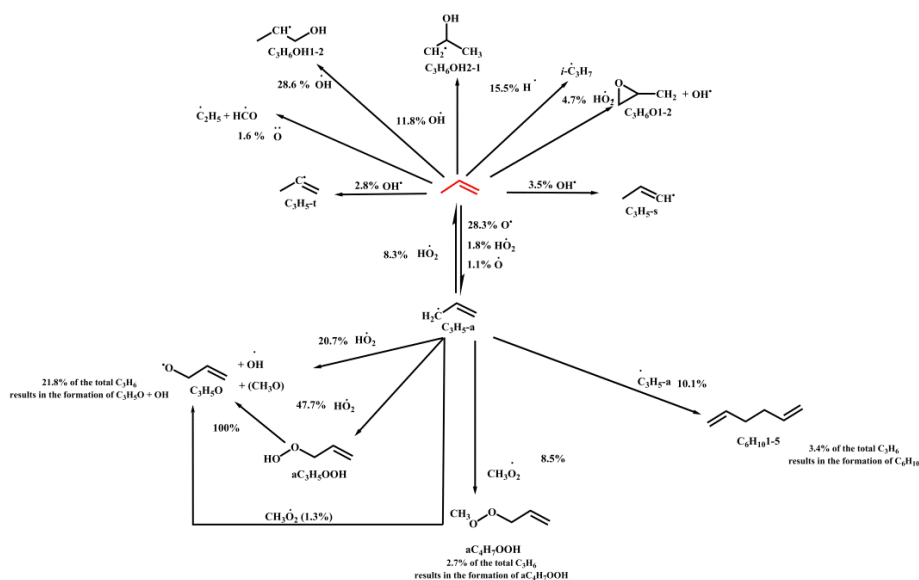
866 Figure 23 : Symbols: HPLFR experimental measurements $p = 15$ atm, $T = 800$ K, lines: current
 867 mechanism predictions, time shifted by 0.28 s and 0.42 to match C₃H₆ mole fractions for figures
 868 a and b, respectively.



869 Figure 24: 0.50% C₃H₆, 2.25% O₂ in N₂, $\phi = 1.00$, $p = 15$ atm, $T = 800$ K. Symbols: HPLFR
 870 experimental measurements, lines: mechanism predictions, time shifted (0.65 s) to match H₂O
 871 profile.



872 Figure 25: 0.62% C₃H₆, 2.25% O₂ in N₂, $\phi = 1.25$, $p = 15$ atm, $T = 800$ K. Symbols: HPLFR
 873 experimental measurements, lines: current mechanism predictions, time shifted (0.70 s) to match
 874 H₂O profile.



875 Figure 26: Flux analysis for the oxidation of a mixture of 0.40% C₃H₆, 5.14% O₂ in N₂, $\phi = 0.35$,
 876 $p = 15.0$ atm, $T = 800$ K mixture at 1.3s.

877 4.2.5. Flux analysis for $\phi = 0.35$, $p = 15$ atm in the HPLFR

878 Many of the reactions are similar to the analysis carried out for the JSR in Fig. 18. However,
 879 under the elevated pressures in the HPLFR a higher percentage of the fuel is consumed via self-
 880 recombination to form 1,5-hexadiene (10.1%) in comparison to the near-atmospheric pressure
 881 experiments studied in the JSR (6.8%) as in Fig. 18. Under this condition of temperature and
 882 pressure, hydroxyl radical addition to propene to form the two \dot{C}_3H_7O radicals (\dot{C}_3H_6OH1-2 and
 883 \dot{C}_3H_6OH2-1) and consumes a significant percentage of the fuel (40%). These radicals react with
 884 molecular oxygen to form propanal and acetone respectively. The reaction between allyl and
 885 methyl-peroxy radical is identified as a consumption pathway for allyl radical. Methyl-peroxy
 886 radical is formed via the pressure dependent reaction of methyl radical and molecular oxygen.

888 5. Conclusions

889 A new chemical kinetic mechanism has been developed to describe the combustion of
890 propene. Important reactions were identified through sensitivity and flux analyses. Rate
891 constants have been adopted from the most comprehensive experimental and theoretical studies
892 where possible. However, for reactions where the literature is lacking, rate constants were
893 estimated. This study includes new estimated rate constants for the reactions of molecular
894 oxygen with propene and with 1- and 2-propenyl radicals. Due to the importance of the reactions
895 of propene and 1- and 2-propenyl radicals with molecular oxygen, further study is
896 recommended. This mechanism has been validated over a wide range of conditions (T , p , ϕ , and
897 % dilution) and shows good agreement with experimental measurements from jet-stirred and
898 flow reactors.

899 The chemical kinetic mechanism has shown significant improvement over a previous version
900 of the mechanism that was validated for C_1 – C_2 chemistry only [32]. This study highlights the
901 importance of only using a chemical kinetic mechanism within its validation limits and offers a
902 contribution to our understanding of small molecule oxidation. The propene sub-mechanism
903 presented herein is intrinsically linked with the C_2 mechanism and vice versa. The effect of the
904 current mechanism on C_1 – C_2 targets is shown in the Supplementary Material and a discussion is
905 included where significant differences exist between the performance of AramcoMech 1.3 and
906 the current mechanism.

907 New experimental measurements for propene oxidation in the JSR at a pressure near 1 atm over
908 an equivalence ratio range of $\phi = 0.64$ – 2.19 are reported. These measurements were obtained at
909 lower temperatures than previously investigated. Some challenges remain with the mechanism
910 performance, as the current kinetic scheme consistently results in the over-prediction of acetone
911 and acetylene and under-prediction propanal, and benzene formed. The mechanism will be
912 developed and improved as further experimental and theoretical data becomes available in order
913 to enhance performance for these species.

914 Speciation profiles were measured in two different flow reactors: the Princeton VPFR and the
915 HPLFR. Data from the VPFR were obtained over the temperature range 843–1047 K and the
916 pressure range 6–12.5 atm for varying equivalence ratios. The data from the HPLFR were
917 obtained at 800 K and 15 atm over a range of equivalence ratios under nearly isothermal flow
918 conditions. HPLFR experiments show that propene exhibits very little reactivity at 800 K and p
919 = 15 atm for $\phi = 1.0$ and 1.25 mixtures. The mechanism can accurately predict fuel and oxygen
920 consumption as well as product formation for both flow-reactors.

921 Tabulated JSR, VPFR, and HPLFR experimental data are included in the Supplementary
922 Material. Also included is a comparison of the performance of the current mechanism against the
923 experimental data presented in this study and in Part II [10] and literature data [3–5,17,77] and
924 the performance of literature mechanisms [5,11, and 32].

925 Part II of this study [10] presents ignition delay time measurements for propene over a
926 pressure range of 2–40 atm, temperature range of 750–1750 K and for equivalence ratios of $\phi =$
927 0.5 to 2.0. Propene flame speed and mass burning rate measurements are also presented in Part
928 II. The ignition and flame data are compared with the chemical kinetic mechanism presented in
929 Part I.

930

931 Acknowledgements

932 Work at Princeton University was supported by the U.S. Department of Energy, Office of
933 Science, Office of Basic Energy Science, both as part of the Combustion Energy Frontier
934 Research Center, an Energy Frontier Research Center funded under award number DE-
935 SC0001198, as well as under award number DE-FG02-86ER13503 administered by the
936 Chemical Sciences, Geosciences, and Biosciences Division. The authors also thank Ms. Lily
937 Zheng for assistance in performing VVPR experiments.

- 940 [1] K. J. Morganti, T. M. Foong, M. J. Brear, G. da Silva, Y. Yang and F. L. Dryer, *Fuel*,
941 108 (2013) 797–811.
- 942 [2] C. K. Westbrook, W. J. Pitz, and H. J. Curran, *J. Phys. Chem. A* 110 (2006) 6912–
943 6922.
- 944 [3] P. Dagaut, M. Cathonnet, and J. C. Boettner, *J. Phys. Chem.* 92 (1988) 661–671.
- 945 [4] T. Le Cong, E. Bedjanian, and P. Dagaut, *Combust. Sci. Technol.* 182 (2010) 333–
946 349.
- 947 [5] S. G. Davis, C. K. Law, H. Wang, *Combust. Flame* 119 (1999) 375–399.
- 948 [6] C. K. Westbrook, W. J. Pitz, *Combust. Sci. Technol.* 37 (1984) 117–152.
- 949 [7] R. Wilk, N. Cernansky, W. Pitz, C. Westbrook, *Combust. Flame* 77 (1989) 145–170.
- 950 [8] T. R. Simonyan, A. A. Mantashya, *React. Kinet. Catal. L.* 17 (1981) 319–322.
- 951 [9] W. Tsang, *J. Phys. Chem. Ref. Data* 20 (1991) 221–273.
- 952 [10] S. M. Burke, U. Burke, R. Mc Donagh, O. Mathieu, I. Osoriom C. Keese, E. L.
953 Peterson, W. Wang, M. Oehlschlaeger, B. Rhodes, R. K. Hanson, D. Davidson, B. W.
954 Weber, C. J. Sung, J. Santner, Y. Ju, E. Volkov, A. A. Konnov, M. Alrefae, F. Khaled,
955 A. Farooq, H. J. Curran. Submitted *Combust. Flame* (2014).
- 956 [11] B. Heyberger, F. Battin-Leclerc, V. Warth, R. Fournet, G. Come, G. Scacchi,
957 *Combust. Flame* 126 (2001) 1780–1802.
- 958 [12] M. Braun-Unkhoff, N. Slavinskaya, and M. Aigner, *ASME Turbo Expo 2010: Power*
959 *for Land, Sea, and Air*, 2010, 2, GT2010–23360, pp. 1037–1047.
- 960 [13] J. Warnatz in *Combustion Chemistry*, ed. W. C. Gardiner; Springer US, 1984; pp.
961 197–360.
- 962 [14] R. Baldwin, R. Walker, *Proc. Combust. Inst.* 18 (1981) 819–829.
- 963 [15] P. Dagaut, M. Cathonnet, J. C. Boettner, *Combust. Sci. Technol.* 83(4-6) (1992) 167–
964 185.
- 965 [16] D. L. Baulch, C. T. Bowman, C. J. Cobos, R. A. Cox, T. Just, J. A. Kerr, M. J. Pilling,
966 D. Stocker, J. Troe, W. Tsang, R. W. Walker, J. Warnatz, *J. Phys. Chem. Ref. Data* 34
967 (2005) 757–1397.
- 968 [17] Y. Hidaka, T. Nakamura, H. Tanaka, A. Jinno, H. Kawano, T. Higashihara, *Int. J.*
969 *Chem. Kinet.* 24 (1992) 761–780.
- 970 [18] R. Fournet, J. C. Bauge, F. Battin-Leclerc, *Int. J. Chem. Kinet.* 31(5) (1999) 361–379.
- 971 [19] CHEMKIN-PRO Release 15101, 2010, Reaction Design: San Diego.
- 972 [20] O. Herbinet, P.-M. Marquaire, F. Battin-Leclerc, R. Fournet, *J. Anal. Appl. Pyrolysis*,
973 78 (2007) 419–429.
- 974 [21] B. Husson, O. Herbinet, P. A. Glaude, S. S. Ahmed, F. Battin-Leclerc, *J. Phys. Chem.*
975 *A* 116 (2012) 5100–5111.
- 976 [22] R. David, D. Matras, *Canadian J. Chem. Eng.* 53 (1975) 297–300.
- 977 [23] J. Tranchant, J. Gardais, *Manuel pratique de chromatographie en phase gazeuse*,
978 Masson, 1982.
- 979 [24] NIST Standard Reference Database 1A, NIST/EPA/NIH Mass Spectral, National
980 Institute of Standards and Technology, 2008.
- 981 [25] S. M. Sarathy, S. Vranckx, K. Yasunaga, M. Mehl, P. Oßwald, W. K. Metcalfe, C. K.
982 Westbrook, W. J. Pitz, K. Kohse-Höinghaus, R. X. Fernandes, H. J. Curran, *Combust.*
983 *Flame* 159 (2012) 2028–2055.
- 984 [26] T. J. Held, F. L. Dryer, *Int. J. Chem. Kinet.* 30 (1998) 805–830.
- 985 [27] Z. Zhao, M. Chaos, A. Kazakov, F. L. Dryer, *Int. J. Chem. Kinet.* 40 (2008) 1–18.
- 986 [28] T. J. Held, F. L. Dryer, *Proc. Combust. Inst.* 25 (1994) 901–908.

- 987 [29] S. Dooley, M. Burke, M. Chaos, Y. Stein, F. Dryer, V. Zhukov, O. Finch, J. Simmie,
988 H. Curran, *Int. J. Chem. Kinet.* 42 (2010) 527–549.
- 989 [30] F. Haas PhD thesis, Mechanical and Aerospace Engineering, Princeton University,
990 2014.
- 991 [31] A. Kéromnès, W. K. Metcalfe, K. A. Heufer, N. Donohoe, A. K. Das, C.-J. Sung, J.
992 Herzler, C. Naumann, P. Griebel, O. Mathieu, M. C. Krejci, E. L. Petersen, W. J. Pitz,
993 H. J. Curran, *Combust. Flame* 160 (2013) 995–1011.
- 994 [32] W. K. Metcalfe, S. M. Burke, S. S. Ahmed, H. J. Curran, *Int. J. Chem. Kinet.* 45
995 (2013) 638–675.
- 996 [33] C. J. Aul, W. K. Metcalfe, S. M. Burke, H. J. Curran, E. L. Petersen, *Combust. Flame*,
997 160 (2013) 1153–1167.
- 998 [34] M. M. Kopp, E. L. Petersen, W. K. Metcalfe, S. M. Burke, H. J. Curran, *J. Propul.*
999 *Power* (2013) Accepted
- 1000 [35] Y. Kochar, J. Seitzman, T. Lieuwen, W. K. Metcalfe, S. M. Burke, H. J. Curran, M.
1001 Krejci, W. Lowry, E. Petersen, G. Bourque In ASME Paper GT2011-45122, 56th
1002 ASME Turbo Expo, 2012.
- 1003 [36] G. Mittal, S. M. Burke, V. A. Davies, B. Parajuli, W. K. Metcalfe, H. J. Curran,
1004 *Combust. Flame* (2013) <http://dx.doi.org/10.1016/j.combustflame.2013.11.005>
- 1005 [37] D. Healy, N. S. Donato, C. J. Aul, E. L. Petersen, C. M. Zinner, Bourque, H. J.
1006 Curran, *Combust. Flame*, 157 (2010) 1526–1539.
- 1007 [38] D. Healy, N. Donato, C. Aul, E. L. Petersen, C. Zinner, G. Bourque, H. J. Curran,
1008 *Combust. Flame* 157 (2010) 1540–1551.
- 1009 [39] D. Healy, M. M. Kopp, N. L. Polley, E. L. Petersen, G. Bourque, H. J. Curran, *Energy*
1010 *Fuels* 24 (2010) 1617–1627.
- 1011 [40] D. Healy, D. M. Kalitan, C. J. Aul, E. L. Petersen, G. Bourque, H. J. Curran, *Energy*
1012 *Fuels*, 24 (2010) 1521–1528.
- 1013 [41] A. Laskin, H. Wang, C. K. Law, *Int. J. Chem. Kinet.* 32 (2000) 589–614.
- 1014 [42] W. K. Metcalfe, S. Dooley, F. L. Dryer, *Energy Fuels* 25 (2011) 4915–4936.
- 1015 [43] G. Jomaas, X. L. Zheng, D. L. Zhu, C. K. Law, *Proc. Combust. Inst.* 30 (2005) 193–
1016 200.
- 1017 [44] H. J. Curran, *Int. J. Chem. Kinet.* 38 (2006) 250–275.
- 1018 [45] J. A. Miller, S. J. Klippenstein, *J. Phys. Chem. A* 117 (2013) 2718–2727.
- 1019 [46] S. S. Vasu, Z. Hong, D. F. Davidson, R. K. Hanson, D. M. Golden, *J. Phys. Chem. A*
1020 114 (2010) 11529–11537.
- 1021 [47] J. Zádor, A. W. Jasper, and J. A. Miller, *Phys. Chem. Chem. Phys.* 11 (2009) 11040–
1022 11053.
- 1023 [48] J. C. Loison, J. Daranlot, A. Bergeat, F. Caralp, R. Mereau, K. M. Hickson, *J. Phys.*
1024 *Chem. A* 114 (2010) 13326–13336.
- 1025 [49] A. Frassoldati, A. Cuoci, T. Faravelli, U. Niemann, E. Ranzi, S. Reinhard, and S.
1026 Kalyanasundaram, *Combust. Flame* (2010) 2–16.
- 1027 [50] M. Scott and R. W. Walker, *Combust. Flame* 129 (2002) 365–377.
- 1028 [51] J. Zádor, S. J. Klippenstein, J. A. Miller, *J. Phys. Chem. A* 115 (2011) 10218–10225.
- 1029 [52] R. Baldwin, C. E. Dean and R. W. Walker, *J. Chem. Soc. Faraday Trans.* 82 (1986)
1030 1445–1455.
- 1031 [53] D. L. Baulch, C. J. Cobos, R. A. Cox, P. Frank, G. Hayman, T. Just, J. A. Kerr, T.
1032 Murrells, M. J. Pilling, J. Troe, R. W. Walker, J. Warnatz, *J. Phys. Chem. Ref. Data*
1033 23 (1994) 847–848.
- 1034 [54] P. Barbé, F. Baronnet, R. Martin, D. Perrin, *Int. J. Chem. Kinet.* 30 (1998) 503–522.
- 1035 [55] N. D. Stothard, R. W. Walker, *J. Chem. Soc. Faraday Trans.* 87 (1991) 241–247.
- 1036 [56] C. F. Goldsmith, S. J. Klippenstein, W. H. Green, *Proc. Combust. Inst.* 33 (2011) 273–

- 1037 282.
- 1038 [57] S. Rolland, J. M. Simmie, *Int. J. Chem. Kinet.* 37 (2005) 119–125.
- 1039 [58] M. A. Oehlschlaeger, D. F. Davidson, R. K. Hanson, *Combust. Flame*, 147 (2006)
- 1040 195–208.
- 1041 [59] H-H. Carstensen, A. M. Dean, *J. Phys. Chem. A* 113 (2009) 367–380.
- 1042 [60] J. D. Savee, O. Welz, C. A. Taatjes, D. L. Osborn, *Phys. Chem. Chem. Phys.* 14
- 1043 (2012) 10410–10423.
- 1044 [61] J. A. Miller, J. P. Senosiain, S. J. Klippenstein, Y. Georgievskii, *J. Phys. Chem. A* 112
- 1045 (2008) 9429–9438.
- 1046 [62] A. Y. Chang, J. W. Bozzelli, A. M. Dean, *Z. Phys. Chem.* 214 (2000) 1533–1568.
- 1047 [63] J. W. Bozzelli, A. M. Dean, *J. Phys. Chem.* 97 (1993) 4427–4441.
- 1048 [64] S. J. Klippenstein, Y. Georgievskii, J. A. Miller, J. A. Nummela, B. K. Carpenter, P.
- 1049 R. Westmoreland In *Proceedings of the Third Joint Meeting of the U. S. Sections of*
- 1050 *The Combustion Institute*, 2003.
- 1051 [65] P. T. Lynch, C. J. Annesley, C. J. Aul, X. Yang, R. S. Tranter, *J. Phys. Chem. A* 117
- 1052 (2013) 4750–4761.
- 1053 [66] A. Fridlyand, P. T. Lynch, R. S. Tranter, K. Brezinsky, *J. Phys. Chem. A* 117 (2013)
- 1054 4762–4776.
- 1055 [67] J. P. Orme, H. J. Curran, J. M. Simmie, *J. Phys. Chem. A* 110 (2006) 114–131.
- 1056 [68] W. Pitz, C. Naik, T. N. Mhaoldúin, C. Westbrook, H. Curran, J. Orme, J. Simmie,
- 1057 *Proc. Combust. Inst.* 31 (2007) 267–275.
- 1058 [69] T. Ingham, R. Walker, R. Woolford, *Proc. Combust. Inst.* 25 (1994) 767–774.
- 1059 [70] P. Dagaut, J-C. Boettner, M. Cathonnet, *Int. J. Chem. Kinet.* 22 (1990) 641–664.
- 1060 [71] S. G. Davis, C. K. Law, H. Wang, *J. Phys. Chem. A* 103 (1999) 5889–5899.
- 1061 [72] N. Hansen, J. A. Miller, P. R. Westmoreland, T. Kasper, K. Kohse-Höinghaus, J.
- 1062 Wang, T. A. Cool, *Combust. Flame* 156 (2009) 2153–2164.
- 1063 [73] R. Atkinson, S. M. Aschmann, *Int. J. Chem. Kinet.* 16 (1984) 259–268.
- 1064 [74] R. Atkinson, S. M. Aschmann A. M Winer, J. N Pitts, *Int. J. Chem. Kinet.* 14 (1982)
- 1065 507–516.
- 1066 [75] C. F. Goldsmith, G. R. Magoon, W. H. Green, *J. Phys. Chem. A* 116 (2012) 9033–
- 1067 9057.
- 1068 [76] S. M. Burke PhD thesis, School of Chemistry, NUI Galway, 2013.
- 1069 [77] Z. Qin, H. Yang, W. C. Gardiner, *Combust. Flame* 124 (2001) 246–254.